A Diagnostic Ice–Ocean Model

W. D. HIBLER III

Thayer School of Engineering, Dartmouth College, Hanover, NH 03755

K. BRYAN

Geophysical Fluid Dynamics Laboratory, Princeton University, Princeton, NJ 08540

(Manuscript received 13 February 1986, in final form 15 December 1986)

ABSTRACT

A coupled ice–ocean model suitable for simulating ice–ocean circulation over a seasonal cycle is developed by coupling the dynamic thermodynamic sea ice model of Hibler with a multilevel baroclinic ocean model (Bryan). This model is used to investigate the effect of ocean circulation on seasonal sea ice simulations by carrying out a simulation of the Arctic, Greenland and Norwegian seas. The ocean model contains a linear term that damps the ocean's temperature and salinity towards climatology. The damping term was chosen to have a three-year relaxation time, equivalent to the adjustment time of the pack ice. No damping, however, was applied to the uppermost layer of the ocean model, which is in direct contact with the moving pack ice. This damping procedure allows seasonal and shorter time-scale variability to be simulated in the ocean, but does not allow the model to drift away from ocean climatology on longer time scales.

For the standard experiment, an initial integration of five years was performed at one-day time steps and a 1.45° by 1.45° resolution in order to obtain a cycle equilibrium. For comparison, a five-year simulation with an ice-only model, and shorter one-year sensitivity simulations without surface salt fluxes and without ocean currents, were also carried out. Input fields consisted of climatological surface air temperatures and mixing ratios, together with daily geostrophic winds from 1979.

The surface current structure at the end of the five-year simulation exhibits a stronger East Greenland Current and Beaufort Sea Gyre than the initial geostrophic estimates, and is in better agreement with observation. In the Greenland/Norwegian Sea the upper 0.5 km of the ocean becomes more isothermal, with a noticeable seasonal variation in temperature. This neutral density allows monthly averaged winter heat fluxes as large as 350 W m^{-2} to be delivered to the upper ocean, thus yielding a much more realistic ice edge than is obtainable by the ice-only model. Spatial variations in ice thickness and ice drift prediction are also in better agreement in the full ice–ocean model as compared to the ice-only model. Except in very shallow regions, month-to-month fluctuations in ice motion are much larger than upper ocean current fluctuations, which also tend to be smaller than mean annual currents. In the central basin, the ice interaction is found to reduce by about 40% the wind stress transferred into the ocean.

Analysis of the advance and retreat of the East Greenland ice edge shows that while there is some initial freezing in the fall, on a monthly averaged basis the ice tends to melt during the winter, thus partially off-setting the advection of ice into the region. The amount of melt tends to oscillate from month to month, with large melt ratios coinciding with large oceanic heat fluxes and vice versa. Examination of shorter sensitivity simulations shows this realistic ice edge to be especially dependent on the inclusion of the full three-dimensional circulation in the ocean, and to a lesser degree sensitive to the inclusion of ice melt fluxes. Analysis of the global budgets shows that an annual northward heat transport across the Denmark Strait and Iceland–Faeroe–Shetland passages of about 0.18×10^{15} W is required to balance the atmospheric heat gain.

1. Introduction

In the polar regions, ocean circulation and the growth, drift and decay of sea ice are closely coupled. To model this coupled system requires consideration of both lateral and vertical circulation in the ocean in conjunction with sea ice dynamics and thermodynamics. On seasonal time scales climate models including sea ice have mainly utilized one-dimensional mixed layer models of the ocean (Manabe and Stouffer, 1980; Washington et al., 1980), in some cases including a mixed layer of variable thickness (Pollard et al., 1983). The main exception to these examples are studies by Semtner (1976, 1986) of the Arctic Ocean circulation. While employing an ocean model very similar to that used here, Semtner's (1976) study did not utilize an interactive ice cover, and mean annual rather than daily wind forcing data were used. More recently, however, Semtner (1986) has extended his model to include a simplified version of the ice model dynamics used here applicable to mean annual or mean monthly atmospheric forcing. On shorter time scales, of the order of a few days, coupled ice–ocean models have been constructed for the ice margin (Røed and O'Brien, 1983).

However, these models have been mainly mechanistic in nature, with idealized ice edge geometry and simplified ice and ocean dynamic parameterizations.

In order to develop a model suitable for seasonal simulations driven by daily time varying forcing, this paper presents a numerical framework for a more general coupled ice–ocean model in which full ice and ocean dynamics are included. While preliminary results from this study were briefly described earlier (Hibler and Bryan, 1984), this paper presents the first full description of the model. Since our main concern in this study is examining the effect of ocean circulation on seasonal simulations of sea ice, observed temperature and salinity data are used to "weakly" force the climatological aspects of the ocean model so that its equilibrium time scale is similar to that of the ice model. Shorter-term variations are, however, prognostically simulated. Consequently, in addition to being useful for basinwide seasonal simulations, the diagnostic model described here should also be useful for mesoscale dynamic studies, for ice–ocean forecasting applications, and for GCM-based atmospheric simulations.

While the concept of a diagnostic model is not a new one, the model described here treats the upper boundary conditions differently than has been done in earlier studies. The basic idea in a diagnostic model is to use available temperature and salinity data to force these aspects of the ocean rather than have the model fully simulate them. This approach was used by Cox (1975) in early investigations of the evolution of baroclinic features in ocean circulation, and by Holland and Hirschman (1972) to examine the role of bottom topography in the circulation of the North Atlantic Ocean. Diagnostic forcing only at the surface was employed by Bryan and Lewis (1979), in an otherwise prognostic simulation of the world ocean. Specification of the background temperatures and salinity fields, with certain error allowances, was employed by Olbers et al. (1986) in conjunction with the B spiral method in order to deduce currents in the North Atlantic. A relaxation procedure similar to that used in this study was introduced in the "robust diagnostic model" of Sarmiento and Bryan (1982) in a study of North Atlantic circulation. The term "robust" was intended to distinguish it from previous, linearized diagnostic models, which proved to be very sensitive to input data.

The present model differs from that of Sarmiento and Bryan (1982) in that the upper surface salt, heat and momentum exchanges are dictated by a sea ice model which includes the uppermost level of the ocean, where no diagnostic relaxation is used. In the absence of local ice cover these fluxes are calculated from bulk aerodynamic formulas using prescribed atmospheric temperatures, humidity and wind. As a consequence of these upper boundary conditions, and the three-year time constant used to damp subsurface temperature and salinity in the ocean towards observations, the model is allowed to respond to high frequency variability in surface fluxes. At the same time it is not allowed to drift slowly away from climatology in the deeper layers of the model ocean. Thus, the ocean component of the model can be thought of as prognostic in its response to high frequency forcing, but diagnostic in its low frequency behavior. Because of the emphasis on simulating the upper boundary exchanges on daily time scales, this model has applicability to climatic sensitivity and long range forecast studies, where fixed specification of the lower boundaries is too restrictive a condition.

To a large degree this study was motivated by the fact that no daily forced seasonal simulation of the Arctic sea ice cover including full ocean circulation has been carried out. The main purpose of this study is to determine the degree to which the inclusion of ocean circulation improves the simulated ice characteristics and where the ice–ocean coupling characteristics are most pronounced. In a larger sense, analysis of this diagnostic model also yields insights into necessary changes (and into the utility) of this type of coupled model for "prognostic simulations" where the ocean characteristics are more fully simulated.

2. Model description

The approach used in constructing this ice–ocean model was to couple an existing two-level dynamic thermodynamic sea ice model (Hibler, 1979; 1980a) with a multilevel baroclinic ocean model (Bryan, 1969). The sea-ice model supplies heat flux, salt flux and momentum exchange boundary conditions for the top of the ocean. The ocean model, in turn, supplies current and heat exchange information to the ice model. The main forcing fields for this coupled model consist of atmospheric wind, surface air temperature, and humidity. Since our main concern here is examining the effect of ocean circulation on sea ice, a fully predictive model of the ocean is not attempted. Instead, mean annual observed ocean temperature and salinity from the Levitus (1982) dataset are used to constrain the model at all levels below the mixed layer. The damping constant has a time scale of three years, which is similar to the time required for the ice model (e.g., see Hibler, 1979) to equilibrate to imposed boundary conditions.

a. Momentum equations

The momentum balance equations for any element of the ice–ocean model are (in rectangular coordinates)

$$m\frac{\partial \mathbf{u}}{\partial t} = mf\,\mathbf{k}\times\mathbf{u} + \tau_a + \tau_w - \nabla_H p(0) + \mathbf{F} \qquad (1)$$

for the ice model and

$$\frac{\partial \mathbf{U}}{\partial t} + \mathbf{U}\cdot\nabla_H\mathbf{U} + w\frac{\partial \mathbf{U}}{\partial z} = f(\mathbf{k}\times\mathbf{U}) - \frac{1}{\rho_0}\nabla_H p + K_M\frac{\partial^2 U}{\partial z^2} + A_M\nabla_H{}^2\mathbf{U} + \delta(z)(\tau_a + \mathbf{F}) \qquad (2)$$

for the ocean model. In these equations $\mathbf{u}(\mathbf{x})$ is the ice velocity, $\mathbf{U}(\mathbf{x}, z)$ the horizontal ocean velocity, $w(\mathbf{x}, z)$ the vertical ocean velocity, f the coriolis parameter, m the ice mass per unit area, $p(\mathbf{x}, z)$ the depth-dependent pressure determined from a "rigid lid" surface pressure plus density variation, τ_a, τ_w the air and water stresses on the ice, $\mathbf{F}$ the force due to internal ice stress, K_M the vertical eddy viscosity, A_M the horizontal eddy viscosity, and $\mathbf{k}$ the unit normal in the z-direction. The force $\mathbf{F}$ due to internal ice stress is calculated using a nonlinear "viscous plastic" constitutive law with the strength proportional to the ice thickness and exponentially related to the compactness (see Hibler, 1979). The strength proportionality constant is the same as used by Hibler and Walsh (1982).

Note that the ice system is only two-dimensional, hence no dirac delta function appears in the air stress plus ice interaction. A second point is that the integrated ocean motion includes the ice motion in a vertically averaged sense. The air and water stress terms in the ice equations are given by

$$\tau_a = \rho_a c_a |\mathbf{U}_g| (\mathbf{U}_g \cos\phi + \mathbf{k} \times \mathbf{U}_g \sin\phi) \tag{3}$$

$$\tau_w = \rho_w c_w |\mathbf{U}_w - \mathbf{u}| [(\mathbf{U}_w - \mathbf{u}) \cos\theta + \mathbf{k} \times (\mathbf{U}_w - \mathbf{u}) \sin\theta], \tag{4}$$

where $\mathbf{U}_g$ is the geostrophic wind (assumed to be larger than the ice motion), $\mathbf{U}_w$ the oceanic surface current, c_a and c_w air and water drag coefficients, ρ_a and ρ_w air and water densities and ϕ and θ air and water turning angles. This boundary layer formulation (McPhee, 1978) normally assumes a spatially invariant boundary layer so that the current beneath the boundary layer is also equal to the geostrophic surface current. However, for simplicity we take $\mathbf{U}_w$ here to be approximated by $\mathbf{U}(\mathbf{x}, z)$ in the second level of the ocean model. For the purposes of the model described here, this is adequate. However, with this approximation, rapid variations in density of the boundary layer are not taken into account. It is also notable that this boundary layer drag is only applicable to steady drag over a time scale larger than inertial oscillations (see McPhee, 1978). In this model such oscillations are not of interest and are purposely over-damped.

An important feature of this model is that the stress transmitted into the ocean is equal to the wind stress plus the ice stress force. Consequently, if there is no ice interaction then the motion of the ocean will be unchanged so long as the air–ocean water drag is unchanged. This feature is physically reasonable. However, it is different than the assumption that the stress into the ocean is equal to the water drag on the ice τ_w. The difference arises due to the convergence of the ice, which can be significant. The main point here is that in a full three-dimensional ocean model the wind stress curl is transmitted to the deep ocean by Ekman convergence, which then exerts a pressure stress on the deep ocean. In an ice-covered ocean the convergence of ice (if the ice is treated separately) must also be considered in the Ekman convergence.

The various forces and directions of ice and water motion (uppermost layer of the ocean) for a given internal ice stress are shown in Fig. 1. Note that the ice motion (or surface water motion) tends to be to the left of the average Ekman transport, a fact verified many times by observation. Also, since (usually but not always) the internal ice stress tends to oppose the ice motion, it will tend to reduce the turning angle between the ice motion and the wind.

In the ocean momentum equations the subgrid scale processes are parameterized via a constant vertical eddy viscosity of $K_M = 1.0\ \text{cm}^2\ \text{s}^{-1}$ and a constant horizontal eddy viscosity of $A_M = 10^9\ \text{cm}^2\ \text{s}^{-1}$. While the first constant is of a physically realistic magnitude, the horizontal eddy viscosity is determined from computational considerations.

b. *Conservation equations*

The main ice conservation equation is

$$\frac{\partial h}{\partial t} = -\nabla_H \cdot (\mathbf{u}h) + S_h(h, A) + \text{Diffusion}, \tag{5}$$

where h is the average ice thickness per unit area (proportional to the ice mass) and S_h is a thermodynamic source or sink term. A secondary continuity equation is carried for the ice compactness A, according to

$$\frac{\partial A}{\partial t} = -\nabla_H \cdot (\mathbf{u}A) + S_A + \text{Diffusion}. \tag{6}$$

More details on the S_A and diffusion terms may be found in Hibler (1979). The ocean conservation equations are given by

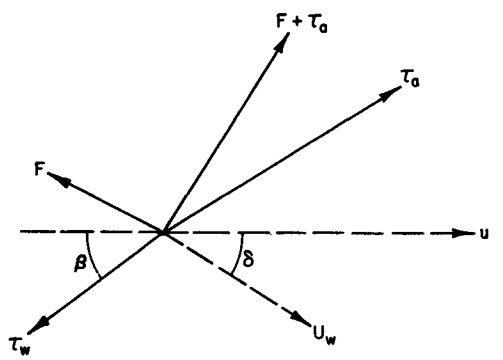

FIG. 1. Vector diagram showing relative directions of ice (u) and Ekman drift ($\mathbf{U}_w$). Also shown are force vectors for the air stress (τ_a) and water stress (τ_w) on the ice, together with a typical internal ice stress force (F). Note that the ideal Ekman drift will be perpendicular to the vector sum of $\mathbf{F} + \tau_a$, whereas the ice drift will be directed at a smaller angle to the air stress, due mainly to the water drag term arising from boundary layer Reynolds stresses.

$$\frac{\partial}{\partial t}(T)+\nabla_H\cdot(T\mathbf{U})+\frac{\partial}{\partial z}(Tw)=\frac{\partial}{\partial z}\left(K_H\frac{\partial T}{\partial z}\right)$$
$$+A_H\nabla_H{}^2T+g(h,A)\delta(z)R_0\theta(T-T_f)-R_t(T-T_0) \quad (7)$$

$$\frac{\partial}{\partial t}(S)+\nabla_H\cdot(S\mathbf{U})+\frac{\partial}{\partial z}(Sw)=\frac{\partial}{\partial z}\left(K_H\frac{\partial S}{\partial z}\right)$$
$$+A_H\nabla_H{}^2S-S_h(h,A)\delta(z)(0.035)-R_t(S-S_0). \quad (8)$$

In these equations $g(h, A)$ is the growth rate of ice in a grid cell with mean ice thickness h and compactness A. For $h = 0$, $g(h, A)$ is the heat exchange in or out of the boundary in the absence of ice. On the other hand, S_h is only equal to the amount of heat exchange used to actually freeze or melt ice. The symbol R_0 is the ratio of the latent heat of fusion of sea ice to the heat capacity of water, and $\theta(x) = 1$ for $x \geq 0$ and 0 otherwise. Also, T_f is equal to the freezing temperature of seawater. The relaxation to climatological temperature and salinity, T_0 and S_0, is done by the terms $R_t(T - T_0)$ and $R_t(S - S_0)$ where R_t is an inverse time constant taken to be 0.333 yr^{-1}, except in the upper layer of the ocean or near "open" boundaries. The growth rate S_h is given by

$$S_h = f(h/A)A + f(0)(1 - A),$$

where $f(h)$ is the growth rate of ice of thickness h (or open water when $h = 0$) and, together with $g(h, A)$, is determined from a full heat budget calculation using bulk aerodynamic formulas for sensible and latent heat exchanges together with incoming longwave and shortwave radiation and a constant conductivity through the ice. More specifics are given in Hibler (1980a). Basically, the surface source term in the temperature conservation equation is equal to the heat transferred through the atmosphere–ocean boundary into the upper layer of the ocean. The surface salt flux into the ocean, on the other hand, is simply equal to the growth rate of the ice multiplied by the average salinity of seawater. It should be noted that this salt flux formulation was chosen because it is globally conservative. It does, however, neglect the fact that sea ice retains a small amount of salt when ice forms, and then slowly decreases the salt content through brine drainage. To properly formulate this process in a globally conservative manner would require an additional salt continuity equation to be added to the ice evolution equations.

The precise way the growth rates and exchanges are determined is easier to envision by considering a finite depth fully mixed layer as is done in the numerical calculations—schematically shown in Fig. 2. The assumption here is that the shear between the ice and the water will mix the mixed layer, and hence the mixed layer will be at the freezing temperature when any ice is present. The ocean transfers heat to the ice by warming up the mixed layer. If ice is present this heat is used to melt ice until the mixed layer returns to freezing, or to warm up the mixed layer if no ice is present. The ice model in turn is used to calculate energy exchanges with the atmosphere, based on the use of a complete surface heat budget. Note, however, that in the presence of ice all of these exchanges do not transfer heat from the ocean to the atmosphere; rather, they transfer heat to the atmosphere at the expense of the latent heat of fusion of seawater via ice formation.

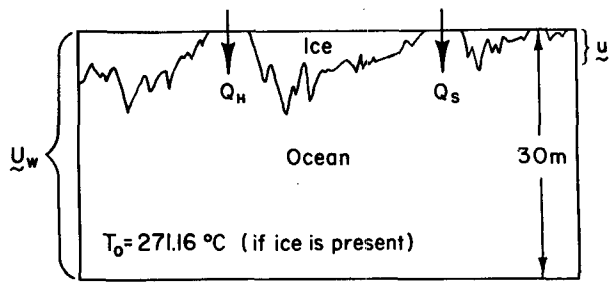

FIG. 2. Schematic diagram of the upper 30 m layer of the ocean, together with ice. Note that the average motion of the upper layer of the ocean (U_w) includes the ice, and that the ice motion $\mathbf{u}$ is taken to be the same for all the different ice thicknesses in a given grid cell. Q_H and Q_S represent schematic surface heat and salt fluxes into or out of the upper mixed layer.

In the ocean conservation equations, the subgrid scale eddy diffusion is parameterized by constant diffusion constants of $K_H = 10.0$ cm^2 s^{-1} and $A_H = 10^7$ cm^2 s^{-1}. This value of A_H was chosen to suppress computational noise and may be physically too large. Density was computed from an empirical equation of state (Bryan and Cox, 1972). In addition, convective processes are treated by employing a convective adjustment whenever the vertical density structure becomes gravitationally unstable.

c. *Numerical framework*

These coupled simultaneous equations were solved as an initial value problem using finite difference techniques. The numerical methods for the separate models are described elsewhere in some detail (Hibler, 1979; Bryan, 1969). Here we concentrate on the time-marching coupling procedure. This procedure for the momentum balance may be illustrated by considering the simplified one-dimensional equations

$$\frac{\partial u}{\partial t}=F(u)+\frac{\partial p}{\partial x}-D(u-U)+\tau_a \quad (9)$$

$$\frac{\partial U}{\partial t}=\frac{\partial p}{\partial x}+[F(u)+\tau_a]. \quad (10)$$

In the case that a leapfrog time-stepping procedure is used, the coupling is as follows:

$$u^{i+1}-u^{i-1}=2\Delta t\left[F(u^{i+1})+\frac{\partial p^i}{\partial x}-D(u^{i-1}-U^{i-1})+\tau_a{}^i\right] \quad (11)$$

$$U^{i+1} - U^{i-1} = 2\Delta t\left[\frac{\partial p^{i+1}}{\partial x} + (F(u^i) + \tau_a{}^i\right]. \quad (12)$$

Note that the idea is to center the exchange terms in time to the degree possible. The exception here is the ocean velocity term in the ice equations, which was taken to occur at the same time as the ice drag term in the boundary layer drag between the ice and ocean. It should also be noted that the ice model is technically not really being integrated as a leapfrog model as, apart from the ocean current, there is no coupling between the two solutions at alternate time steps at all. Every 19 steps a forward step is used for both models, which eliminates any splitting problems. Details of the integration procedure for the ocean model are given in Bryan (1969) and were recently documented by Semtner (1974) and Cox (1984). The ice model integration procedure and finite differences are given in Hibler (1979) and documented in Hibler (1980b). It is worth noting that carrying out this time-stepping procedure requires a relaxation solution in both models: in the ice model to solve for the highly nonlinear ice interaction term embodied in F, and in the ocean model to solve for $\nabla_H p$ by means of finding the time change in the vertically integrated stream function within the rigid lid approximation. With this rigid lid approximation $\nabla_H p$ does not appear explicitly, but can be deduced from information at hand at the end of the time step, which in this case is necessary for the coupling to the ice model.

The coupling of the ice model and the ocean model conservative equations required a few modifications of the procedure used in the uncoupled model. In particular, at the critical first level both models were integrated forward in time, which then produced a tendency for temperature, salinity, and ice thickness in the upper level. In a splitting procedure the temperature was then set to freezing and an equivalent amount of ice melted, with a commensurate adjustment of the salinity in the upper layer. As a consequence the ice model effectively supplies a given temperature and salinity to the upper layer of the ocean, which is then used by the ocean model as a boundary condition. This implicit procedure ensures conservation and does not allow the ice cover and ocean surface temperature to get out of balance on alternative time steps.

The need for daily forcing to drive the ice model limits the integration time step to one day. However, there are high speed waves in the system, internal gravity waves, and Rossby topographic waves which place a more stringent condition on the time step of the numerical integration. Filtering these waves is possible, since they are not of real interest in the present context. For this purpose, we have chosen to use "distorted physics" (Bryan, 1984), whereby the local derivative with respect to time of the horizontal velocity is multiplied by a coefficient large enough to allow a time step of one day, in this case a factor of 10. This particular distortion factor was largely necessitated by the implicit treatment of the coriolis term which, together with irregular topography in the Arctic Ocean, removes the diagonal dominance of the relaxation solution for large time steps.

d. Grid configuration and forcing fields

The ocean model uses a spherical geometry. To obtain the most uniform spacing over the Arctic Ocean, the equator of the spherical system was aligned with 35°E and passed through the pole (Fig. 3). There is a slight incompatibility with the ice model, which was in Cartesian coordinates, but the distortion is not very great since the grid only extends to a latitude of 60°N in the Greenland–Norwegian Sea. At the pole the two grids exactly coincide, with a spacing of 1.45° × 1.45° in the ocean model and 160 km × 160 km horizontal resolution in the ice model. The main error caused by this geometry difference is in the balance of heat and salinity exchanges (see Appendix A). However, it must be kept in mind that the robust diagnostic model for the ocean does not exactly conserve temperature and salinity, so that the small differences induced by the grid mismatch were not felt to be critical for this study (see Appendix A).

In the ocean model 14 vertical levels are used, with deeper levels having increasing thickness. The thickness and depths of the levels are schematically shown in Fig. 4. Bottom topography is resolved by using differing numbers of levels at different locations. Figure 5 shows the bottom topography in the analysis region of the grid resolved by the model. This topography was obtained by interpolation from global topographic height data compiled by Smith et al. (1966).

The lateral boundary conditions imposed on the ocean model are similar to those used in Sarmiento and Bryan (1982). Rigid walls were imposed along outer grid points. Adjacent to the southern wall, located in the open ocean, observed temperature and salinity were imposed by using a damping constant of only 30 days. With this procedure even the intense vertical motion generated by the closed boundaries did not cause serious departures from the observed water mass distribution. Since this wall was deliberately placed some distance away from the region of primary interest, it was felt that setting the barotropic component of the model equal to zero along the wall would not cause any serious distortion. A special advantage of this type of boundary condition, as opposed to specifying the transports, is that the currents and transports in the Faeroe–Shetland region are simulated and can vary in time. A similar 30-day condition is also used in the Bering Strait region (see hatched grid cells in Fig. 3) in order to yield waters in this region with similar temperature and salinity to observed values.

At all other grid cells in the ocean (below the top layer), diagnostic forcing with a weaker relaxation con-

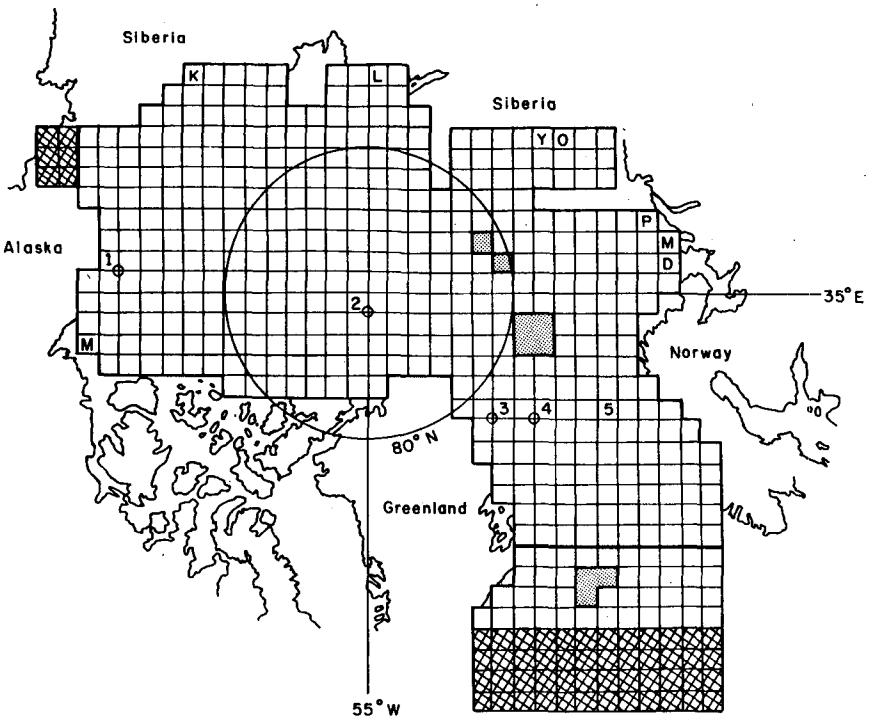

FIG. 3. Grid configuration used for ice–ocean model. The ocean grid is a spherical grid system with the "equator" lying on the 35°E meridian and the "Greenwich" meridian lying along 55°W. In the hatched grid cells a 30 day relaxation to observed data was used. Numbered grid cells and circled grid points denote locations of more detailed analysis, and lettered grid cells denote locations of river inflow (see Table 1).

stant of three years was used for the diagnostic terms in Eqs. 7 and 8. This time constant was chosen to be approximately the same as the ice model equilibrium time constant (e.g., see Hibler, 1979; 1980a). Down to and including level 9 these observed temperature and salinity data were taken from mean annual values compiled by Levitus (1982). However, because of the paucity of data for the deep Arctic regions the deep values of these data in the three major Arctic Basin regions were found to yield unrealistic baroclinic currents, which in turn affected the surface currents. Consequently, levels 10 and deeper were taken to be of constant salinity and temperature with each of the three deep basins having different values for the constants. The constant values were taken from estimates by Coachman and Aagaard (1974).

CENTER DEPTH	DEPTH	LEVEL THICKNESS
	0	
15		30
	30	
53.2		46.3
	76.3	
110.0		67.5
	143.8	
191.0		94.4
	238.2	
302.4		128.5
	366.7	
452.0		170.5
	537.2	
648.2		222.0
	759.2	
900.9		283.5
	1042.7	
1220.8		356.2
	1398.9	
1619.2		440.5
	1839.4	
2107.8		536.8
	2376.2	
2698.5		644.6
	3020.8	
3402.3		763.0
	3783.8	
4229.1		890.7
	4674.5	

FIG. 4. Level depths and thicknesses for ocean model.

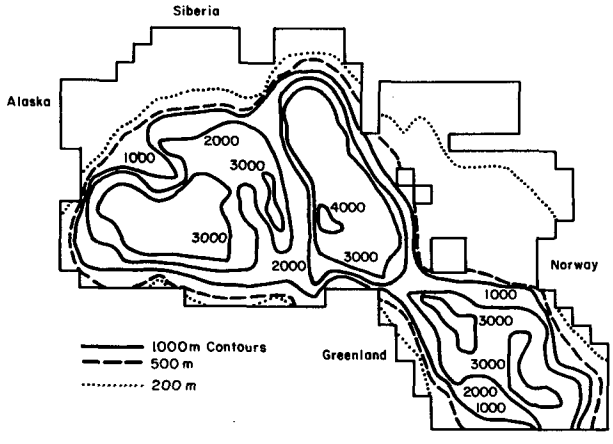

FIG. 5. Contours of topography resolved by the ocean model.

TABLE 1. River inflow (10^3 m^3 s^{-1}).

Mackenzie	(M)	7.9	Kolyma	(K)	3.8
Ob	(O)	12.4	Lena	(L)	15.4
Yenisei	(Y)	17.3	Pechora	(P)	4.1
Dvina	(D)	3.5	Mezen	(M)	0.8

Additional runoff around perimeter of analysis region: 74.3.

For river runoff into the ocean, inflow values from Soviet and Canadian rivers identical to that used by Semtner (1976) were employed, with the difference being that these river runoff values were specified to occur seasonally, with equal amounts from day 171 to 291 (20 June to 18 October). The grid cells in Fig. 3 containing letters denote cells where river runoff is specified, with the river runoff values given in Table 1. In addition, a residual river inflow noted in Table 1 was distributed uniformly around the perimeter of the analysis region just north of Iceland. This perimeter value was also taken to vary in a seasonal manner. Since in a rigid lid model it is not possible to specify changes in volume, this river runoff is specified as a freshwater flux of 35 parts per thousand. A similar fraction was used for ice melt.

Input fields for the ice model consisted of monthly climatological air temperatures and dew points (from Crutcher and Meserve, 1970), together with daily time varying winds taken from the NMC analysis for the "FGGE" year, December 1978 to November 1979. These data were also used to compile daily averaged radiation fields using the parameterizations discussed in Hibler (1980a). Use of daily time varying winds is especially important in driving an ice model, in that much of the air–sea heat exchange arises from leads created by rapid variations in wind forcing. The use of the FGGE year was useful because there were a large number of drifting buoys in the Arctic Basin during this time period which allow a valuable check on the drift rates of the model and which to a limited degree supply better pressure for the analysis fields. However, a possible difficulty with using a given year's forcing field is that the stress can be atypical compared to the mean values, as illustrated by interannual analysis of sea ice simulations performed by Walsh et al. (1985). (The particular difficulty of using the FGGE winds in this context is discussed in Appendix B.) This problem would be especially pronounced for the ocean if the ocean model were allowed to run to a full climatic seasonal equilibrium. However, in the study described here this problem is largely avoided by the use of the diagnostic forcing, which damps the long-term mean ocean circulation to the observed data. Since this procedure does not affect shorter time scales, the upper ocean and ice pack are free to be prognostically simulated by the coupled model (e.g., see Appendix C). In this sense the model is partially diagnostic and partially prognostic.

3. Simulation results

To obtain seasonally varying equilibrium results the coupled diagnostic model was integrated for five years, with the same seasonal wind forcing being repeated each year. For comparison, a five-year simulation was carried out with an ice-only model, which included only a motionless fixed depth, 30 m mixed layer and no ocean currents. In addition, to examine the role of different processes, one-year sensitivity simulations without surface salt fluxes and without ocean currents were carried out. These latter one-year simulations were initialized with ocean and ice conditions at the end of the fourth year of the ice–ocean simulation. For initial conditions for the full ice–ocean simulation, the observed temperature and salinity fields were used, together with initial ice thickness contours shown in Fig. 6. These ice thickness contours were created by assuming a uniform ice thickness of 3 m everywhere, and then melting sufficient ice to either reduce the temperature of the top 30 m layer of the ocean to the freezing temperature or to remove all the ice. [The initial temperatures were taken from the mean annual Levitus (1982) data.] No salt fluxes were assumed from the initial melting, however, since such a strong initial influx would take very long to remove, even with the diagnostic terms in the ocean.

a. Evolution of ice and ocean circulation

The evolution of the overall characteristics of the ocean circulation is illustrated by the evolution of the geostrophic currents. Figure 7 compares the annual averaged pressure differences between level 2 and level 5 for the fifth year of the standard simulations with the initial pressure differences obtained from the Levitus (1982) data. For comparison this figure also shows the surface pressure from the fifth year of the coupled simulation (which aids in identifying barotropic currents)

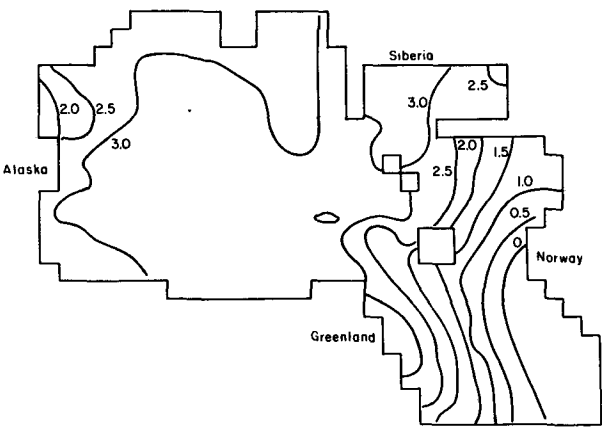

FIG. 6. Initial ice thickness contours (meters) used for coupled ice–ocean simulation.

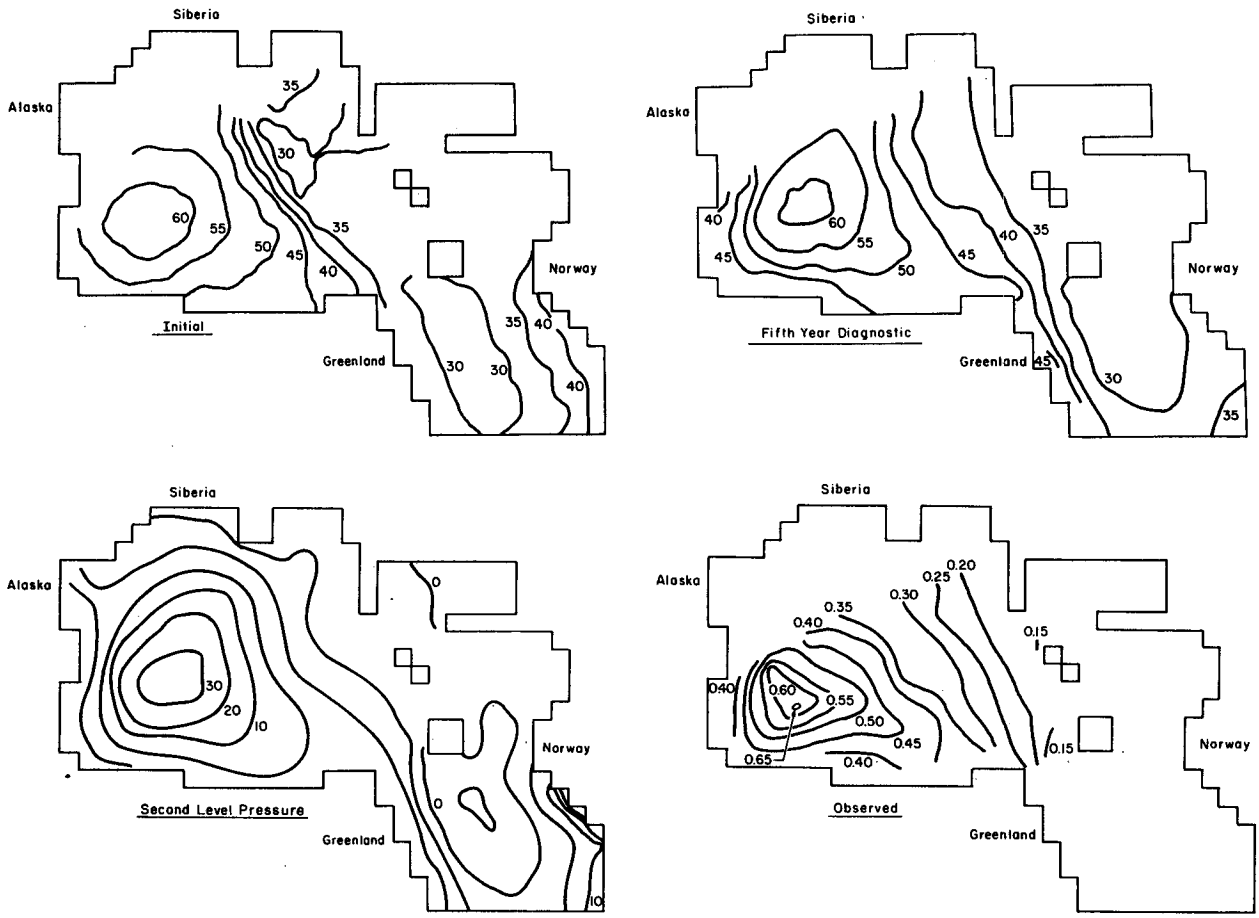

FIG. 7. Pressure differences (in centimeters of water) between the second level and the fifth level in the ocean model at (a) the beginning of the simulation and (b) after five years. The fifth year results represent the mean annual average. Also shown is (c) the mean annual pressure at the second level of the ocean model in the fifth year and (d) observed dynamic height anomalies (in meters) compiled by Coachman and Aagaard (1974) for the central Arctic Basin.

and the observed dynamic height contours obtained by Coachman and Aagaard (1974) for the Arctic Basin. While the overall shape of the geostrophic currents is the same, there is a considerable change in the final solution evolved by the coupled model. In particular, there is an intensification of the gyre motion in the Arctic and of the currents in the East Greenland region. Both these phenomena are in better agreement with Arctic based observations, the first being closer to Coachman and Aagaard's results and the second being verified by buoy drift observations in the East Greenland region (discussed later). Examination of the spinup results (Fig. 8) shows that the first phenomenon primarily occurs early in the simulation and is more a case of the model serving as an inverse analysis of the observed temperature and salinity fields. In particular, geostrophic boundary currents may be inconsistent with smoothed estimates of observed temperature and salinity. These geostrophic currents will cause a readjustment of the density field, which further intensifies the current. This adjustment is a valuable feature of this type of a robust diagnostic model and makes it a useful method for assimilating observed data when there is considerable uncertainty in the data.

Such an adjustment also occurred in the East Greenland region. However, here there is formation of a more pronounced frontal current shear due to the geostrophic adjustment induced by the strong wind. There is, in addition, a small variation in the current due to freshwater fluxes by the ice, which produce a stronger frontal structure in the East Greenland region that tends to somewhat inhibit the southward currents. For the North Slope region, on the other hand, this wind stress is rather weak for this particular year, and the geostrophic adjustment tends to mitigate the current there in a slow manner (Fig. 8).

As can be seen from the surface pressure field, the overall surface currents largely follow the geostrophic currents driven by density variations, with the major exception being a strong barotropic current off the Norwegian coast.

Changes in the vertical density structure are illustrated in Fig. 9, where we have plotted initial and final annual averaged temperature and salinity profiles in

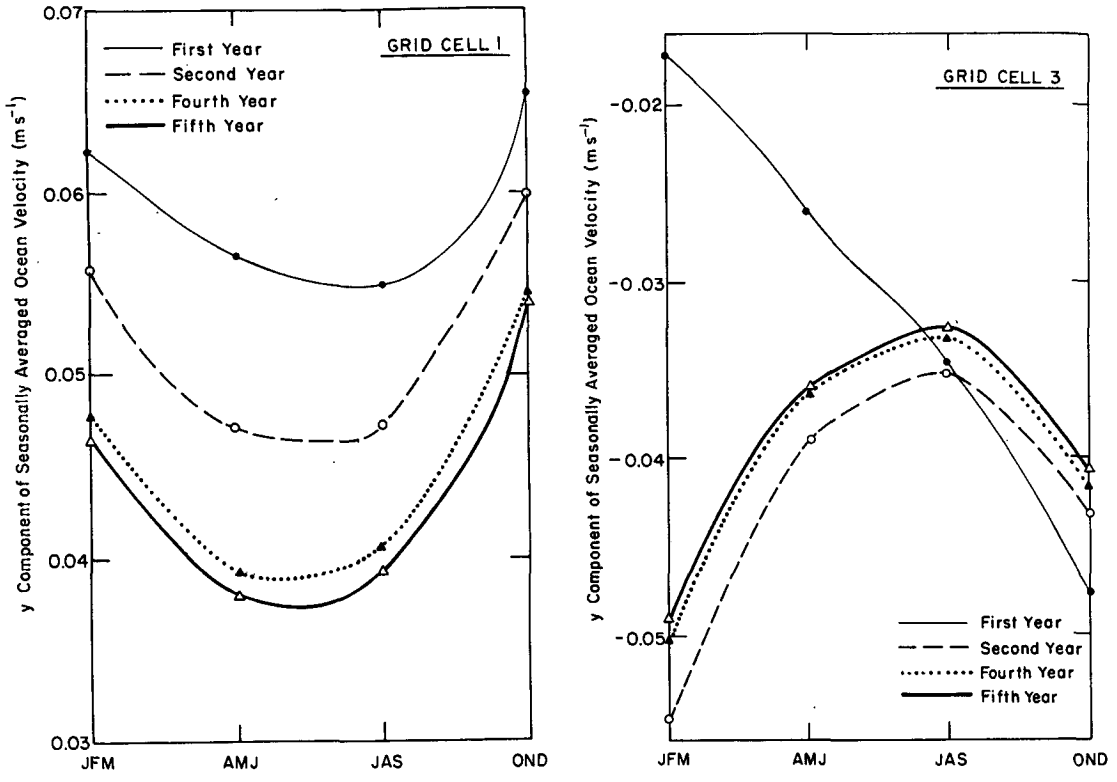

FIG. 8. Seasonally averaged currents at two locations during the spinup process.

the upper 600 m of the ocean at selected locations. In certain regions there is a considerable adjustment due to the faster time scales of the upper ocean allowing it to be effectively modeled even though there are diagnostic source terms being applied. Verification that this adjustment is mainly due to the prognostic character of the ocean model is given in Appendix C.

In the Greenland Sea region there are more major changes associated with ice melt and convective overturning due to cooling. In particular, at grid cell 5 (except for the very top layer, which, due to summer warming, has a higher temperature), the adjusted vertical profile down to about 600 m is neutrally stable, which is due to the intense surface cooling that causes relatively deep convection. This neutrally stable profile, in turn, effectively prevents any ice formation in the ocean by forcing the atmosphere to cool off the ocean down to 500 m. Heat at these depths is brought northward by the lateral transport in the ocean. As one moves nearer the ice edge, however, it is possible to have a cooler temperature near the water surface due to a freshwater lens. Grid cell 4 is a transition zone in this sense and, as discussed later, is close enough to neutral stability that oceanic heat flux fluctuations can occur rapidly in time, due to being triggered or stopped by ice growth and melting. Grid cell 3, on the other hand, is under a region where ice normally occurs and more melt occurs. Here the coupled model creates a more pronounced lens of fresh cold water, with the low salinity preventing convective overturning with the deeper, warmer, saltier water below about 250 m. This characteristic s-shaped curve is in qualitative agreement with ST curves for the north Greenland regions reported by Coachman and Aagaard (1974).

In the central Arctic Basin (grid cell 2) there is very little change in the salinity, with slightly fresher surface water induced by ice melt, and a slight cooling. Off the Beaufort Sea there is a more major change, with the upper layer water being warmer and saltier. Both these Beaufort Sea changes arise from upwelling there, which tends to pull up warmer, saltier water.

Evolution of the ice thickness contours can be determined by comparing Fig. 6 to Fig. 10. In Fig. 10, ice thickness contours for February are plotted for the full and ice-only models. Also shown are observed ice edge contours for the end of February. The full model produces a rather weak buildup against the Canadian Archipelago, where observed data yield very large buildups (see Hibler, 1980a). This weak buildup, together with unrealistically large buildup against the Siberian coast, is due to the somewhat atypical ice transport (e.g., see Walsh et al., 1985) obtained for this year due to this particular year's wind fields (see Appendix B). This feature reflects one of the main problems that arise with the use of a given year for equilibrium simulations. In the ice-only model the absence of ocean

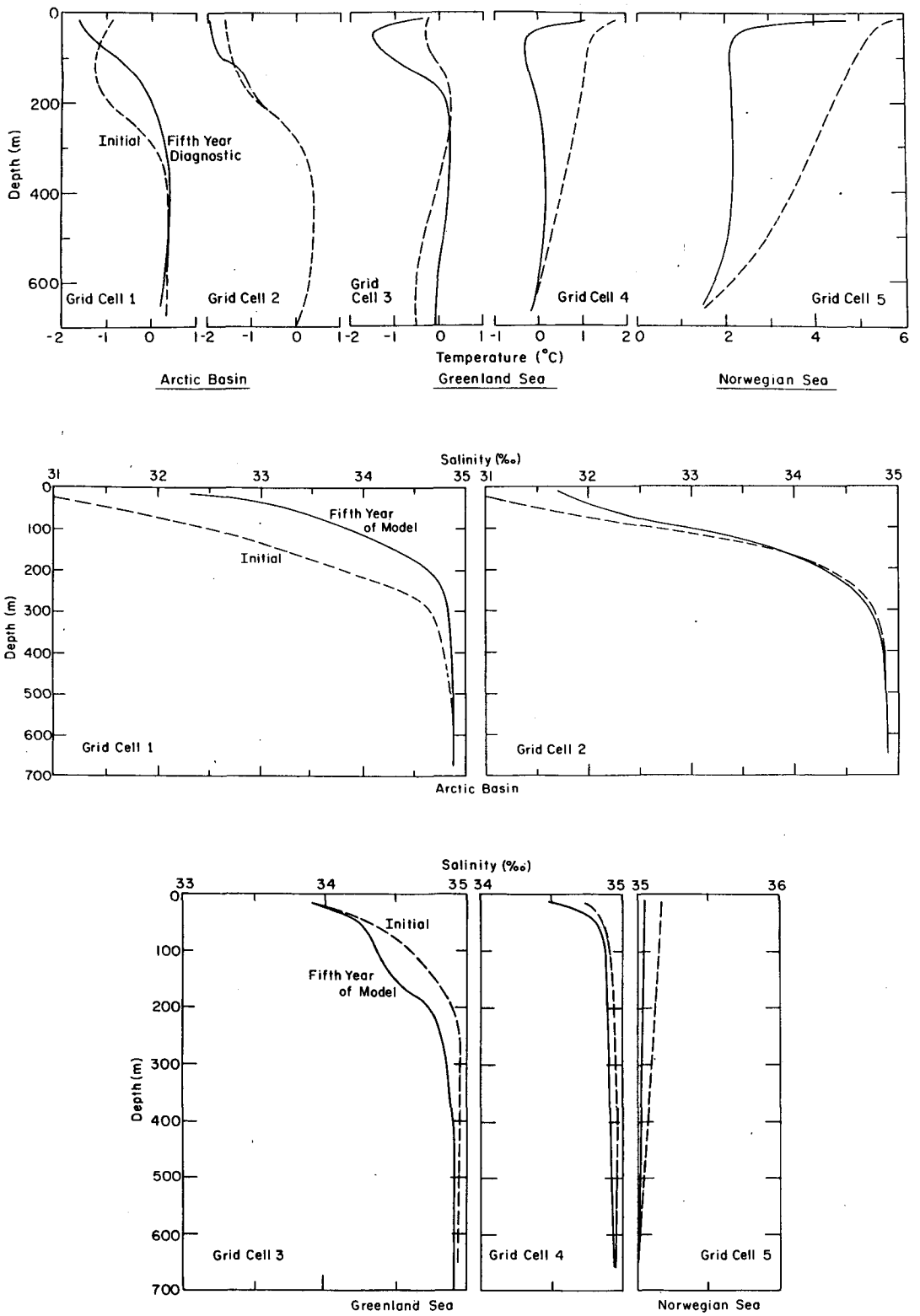

FIG. 9. Initial (dashed) and final (solid) temperature (a) and salinity (b) profiles for the upper ocean at representative locations. The simulated values (solid) represent the annual average of the fifth year of the ice–ocean simulation.

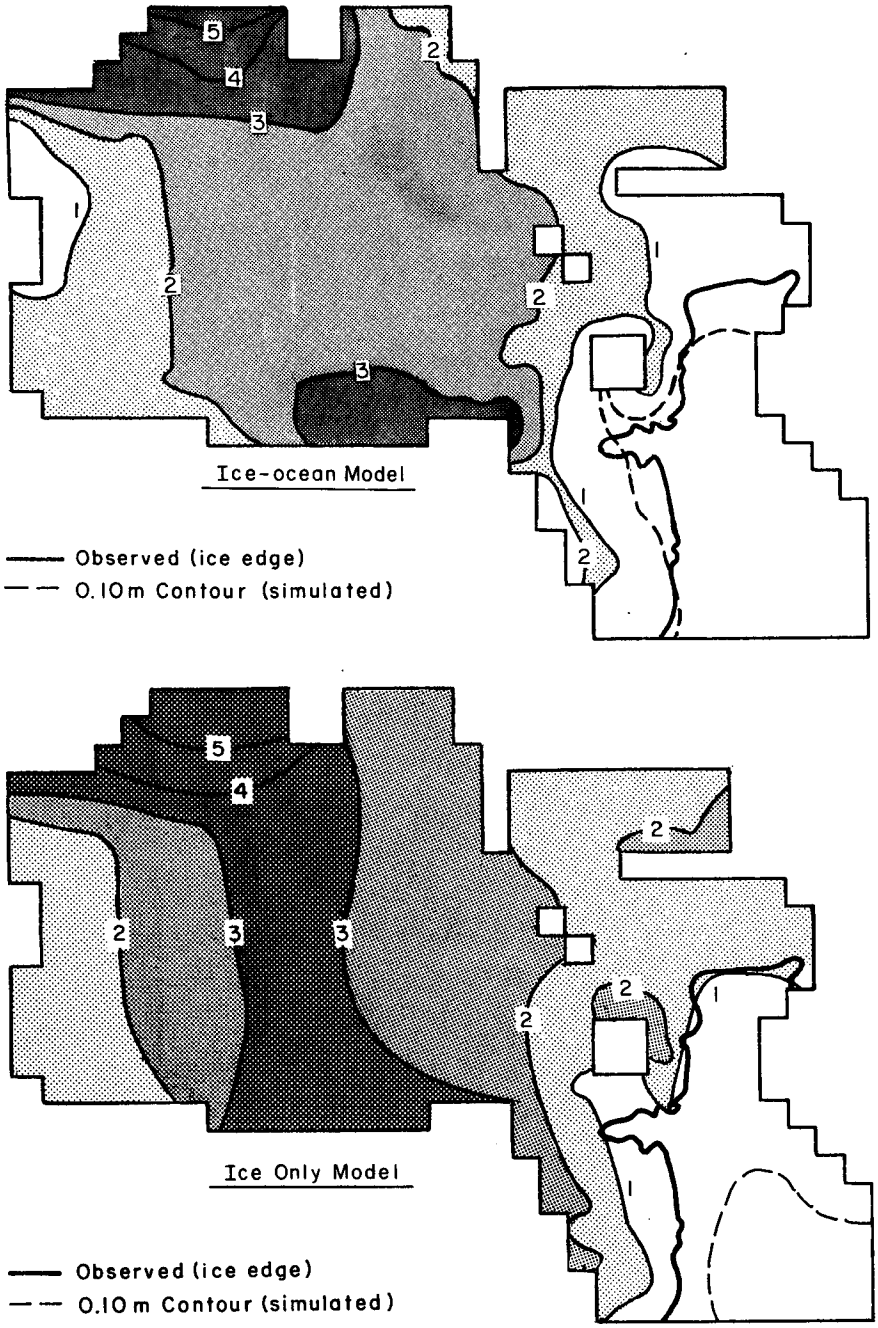

FIG. 10. Average February ice thickness contours (meters) for the coupled ice–ocean model (a) and the ice-only model (b). Also plotted is the observed ice edge for February 1979 (heavy solid line) and the 0.10 m thickness contour (dashed) from the model results.

currents causes an even more unrealistic lack of buildup against Greenland.

However, the most major difference between the ice-only and full models is the ice edge location. This improvement of the ice margin location is due to the large amount of heat that flows from the deeper ocean into the mixed layer in the winter. Spatial and temporal variations of this flux are discussed in more detail below.

b. Ice and ocean velocity characteristics

To examine the relative behavior and interdependence of ice and ocean surface velocities, mean yearly

and monthly values were compiled and compared. In addition, the simulated and observed drift of a number of drifting ice buoys were compiled for both the full coupled model and the ice-only model. The overall surface current and ice drift behavior is shown in Fig. 11, which compares mean annual ice motion and ocean currents at the second level of the ocean model. Ice motion in the absence of ice is also included, which represents free drift of ice of zero mass, or equivalently the drift of the upper few centimeters of an ideal boundary layer. As can be seen, the ocean currents closely follow the surface pressure contours and have a classic gyre pattern commensurate with the observed temperature and salinity fields. The ice motion, on the

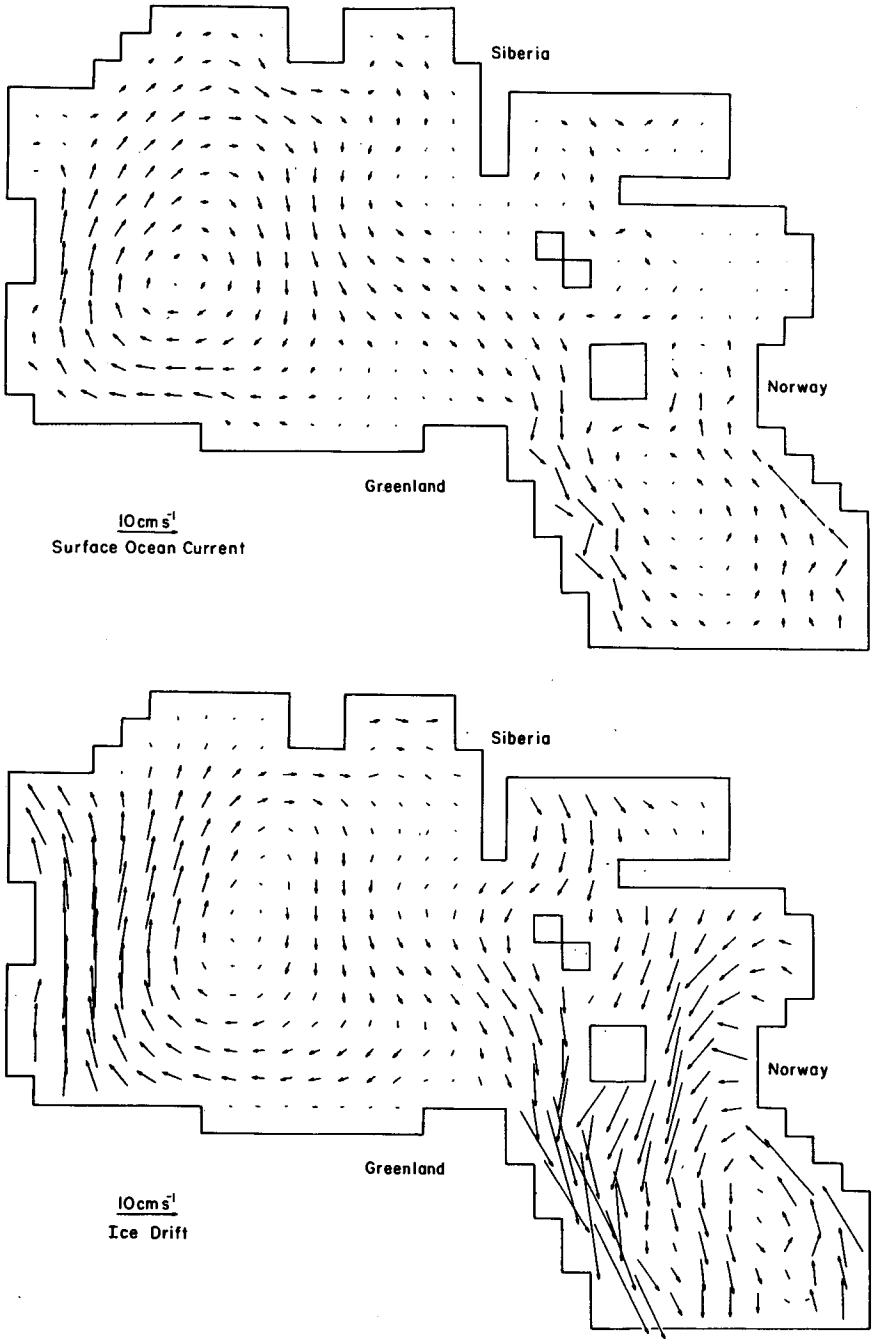

FIG. 11. (a) Mean annual currents at the second level of the ocean model for the fifth year of the coupled simulation and (b) mean annual ice motion.

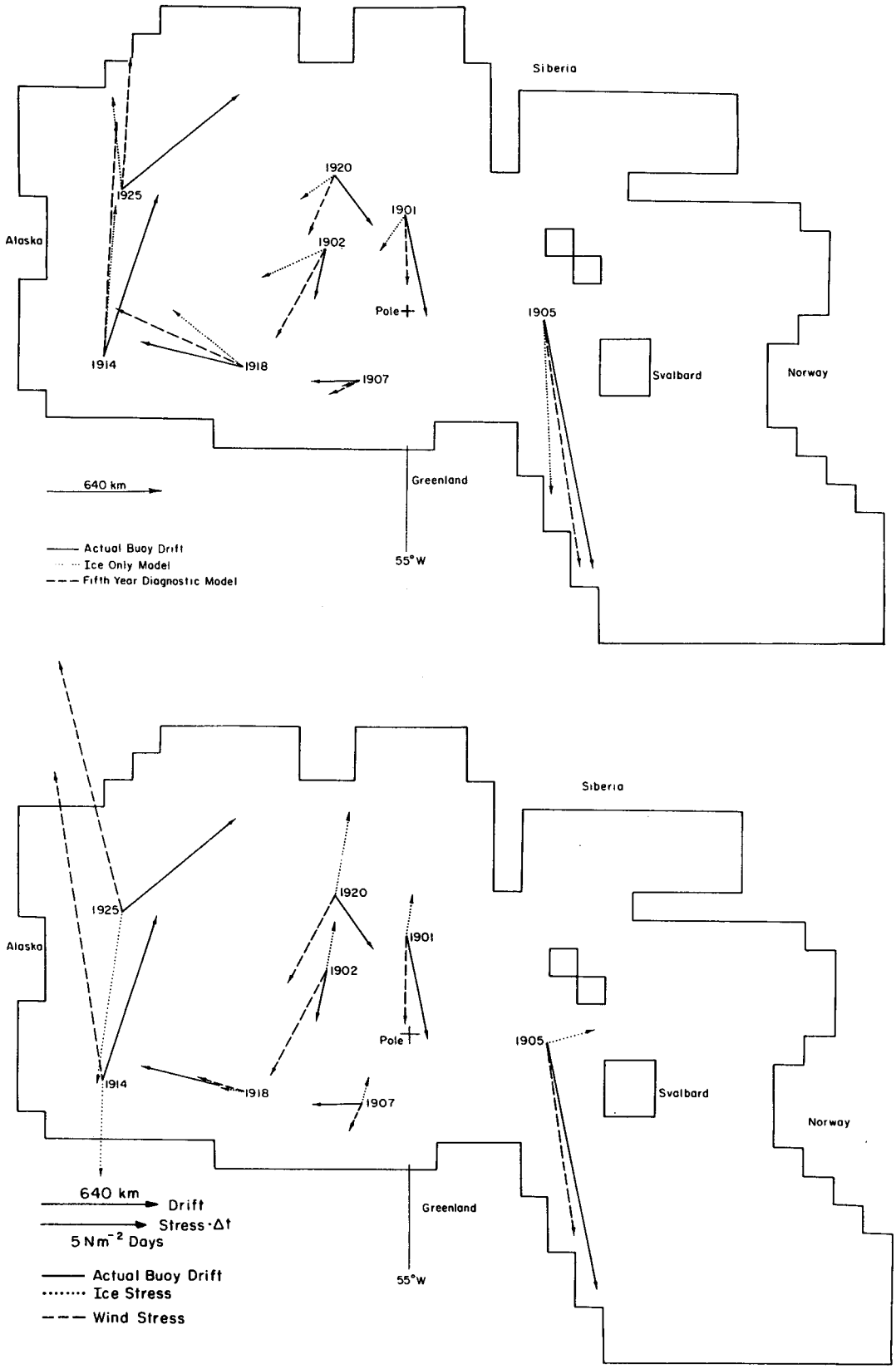

FIG. 12. Long-term averages of (a) simulated and observed drift rates of ice buoys and (b) wind stress and force due to ice interaction at the locations of the ice buoys. Drift rates have been converted to distances by multiplication by time. The time intervals used were February–November for buoys 1901 and 1902, March–September for buoy 1905, May–November for buoy 1907, and March–November for the remaining buoys.

other hand, is more of an elongated, weakened gyre, with very little transpolar drift. This weakened gyre motion is especially apparent in the drift from the ice only simulation discussed in Appendix B. Basically, since ice is at the surface, it does not follow the Ekman drift but more closely parallels the geostrophic wind, a fact known for over 50 years beginning with Nansen (e.g., see Zubov, 1943). Typical values of the ice drift are almost twice as large as the ocean current values.

This long-term fraction of current-induced ice drift is also illustrated by the buoy drift predicted and observed (Fig. 12a). For both the models the average predicted drift was obtained by linearly interpolating the average monthly drift rates to the mean monthly position of the buoy. A similar monthly averaged procedure was used to determine the long-term ice and wind stresses (Fig. 12b) at the locations of the buoys. Overall, the inclusion of the full ocean model consistently improves the predicted drift magnitude and turning angles, and especially improves the simulated drift direction and magnitude of ice drift in the East Greenland Sea. Specifically, for the drift vectors shown in Fig. 12, the average turning angle error in the full model is 23° as compared to 38° for the ice-only model. The drift magnitudes also show an improvement, with an average cumulative error of 45% for the full model as compared to 58% for the ice-only model. (The cumulative drift error is the difference between the net simulated drift magnitude and observed drift magnitude divided by the observed magnitude.) Because random errors are cumulative this net drift measure is a very stringent test of model performance, and the errors obtained here are not unusually large (e.g., see Hibler and Walsh, 1982; Hibler and Tucker, 1979).

Figure 12b illustrates the very significant role that ice stress plays in this model. A more quantitative measure of the percentages is given in Table 2. Note that even though the buoys may be far from shore, the magnitude of the ice interaction vector is typically about 40% of the wind stress. Also, while the ice interaction normally is oriented in opposition to the average wind, that is not always true, as exhibited, for example, by buoy 1918, where the ice stress is on the average aligned with the wind and tends to abet the ice motion. These results tend to contradict the view that ice interaction doest not play a significant role far from shore. While at first glance this may seem counterintuitive, it is quite reasonable when one considers the theory of plastic ice interaction. In a one-dimensional constant strength plastic system (e.g., see Hibler, 1985), the simulated ice drift will asymptotically approach the free drift value for large wind speeds but will be significantly different for small wind speeds. Thus short-term fluctuations in ice drift will tend to follow the wind, while longer-term variations can be more strongly affected by ice interaction. This is one possible reason why the wind and ice drift have such a high coherence at high frequencies, and consequently such a high temporal correlation (Thorndike and Colony, 1982). In general these remarks highlight the need for more detailed sensitivity studies of this type of model, with verification based on more extensive datasets.

TABLE 2. Magnitude of ice interaction at buoy locations.

Buoy	Ratio of average ice stress magnitude to wind stress magnitude
1901	0.44
1902	0.42
1905	0.26
1907	0.81
1914	0.32
1918	0.55
1920	0.86
1925	0.67

While the ocean currents tend to be comparable in magnitude to ice motion in the long term, over the shorter term the ice drift fluctuations are much larger (except in shallow seas). This is illustrated in Fig. 13, which shows time series of monthly averaged ocean currents and ice drift at the circled grid points in Fig. 3. Also shown in this figure are the currents for the one-year sensitivity study without salt fluxes due to ice melting and freezing. As can be seen, the ice variations are quite large in response to the wind. The wind-driven ocean currents, on the other hand, are much smaller due to the depth of the ocean. With less damping in the ocean than employed here it is possible that these current variations, say in East Greenland, could be larger due to variations in the wind stress enclosed by the constant bottom topography contours, as for example suggested by Willibrand et al. (1980). However, the ice is effectively uncoupled in the sense that it can immediately follow the wind. The small changes in the currents, when salt fluxes from the ice were not considered, indicate that these surface flux-induced changes are not so critical on the seasonal time scales in a coarse resolution model. However, over a period of several years these fluxes can modify the stratification and hence current structure (e.g., see Figs. 8 and 9).

That the mean steady currents in most locations are larger than the fluctuations was verified more directly by looking at the daily rms currents (Fig. 14). These are compared to the mean currents along a transect parallel to the x-axis and going through the circled grid point near grid cell 1. The other transect passes through the circled grid points in the East Greenland region and is also parallel to the x-axis. As can be seen, the fluctuating currents tend to scale with the increase of the rate of change of bottom topography, as we would expect from barotropic considerations (Willibrand et al., 1980). In the deep ocean the mean currents are larger. In the shallow shelf regions of the Arctic Ocean (most notably the Barents Sea), the fluctuating currents become dominant, with relatively weak mean currents.

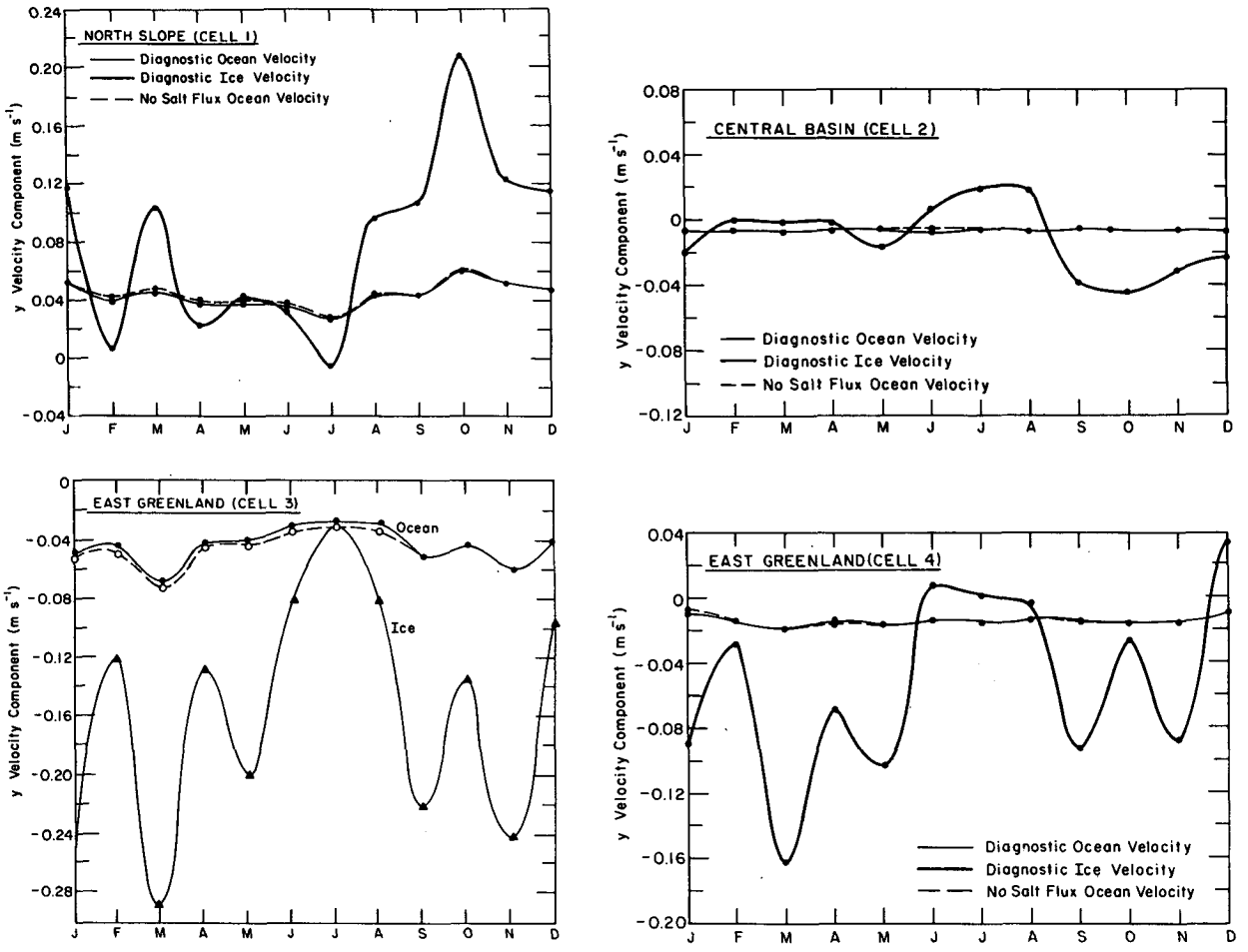

FIG. 13. Time series of y velocity components of ice drift and ocean current velocities at representative locations. The ocean velocities are taken from the second level of the ocean model. Also shown (dashed line) is the velocity from the one-year sensitivity study where the salt fluxes due to ice melt and growth were set equal to zero.

This in turn indicates that ice forecasts in these shallow seas may really require a fully interactive ice–ocean model. Note that the East Greenland region, especially along the shelf break, is a somewhat intermediate situation, with both barotropic and baroclinic currents being important.

c. *Ice edge fluctuations*

As note above, one of the main differences between the fully coupled model and the ice-only model is the behavior of the ice edge in the East Greenland region. A more detailed view of the variation of this edge is shown in Fig. 15, where the 50% concentration limits for the two models are compared to observed values for every other month. (In general, the comparison with observed data should not be expected to be precise, since climatological air temperatures and dew points rather than values for 1979 were used.) As can be seen, the main effect of including the ocean circulation is to yield a more realistic reduced ice extent. This difference between models begins in December (or November) as the ice rapidly advances and persists through to April. Basically, the stratified nature of the ocean out to approximately the ice limit causes the advance up to about December to be similar to that predicted by a simple fixed depth boundary layer so that the advance of both models up to this point is much the same. Beyond that point, the convective overturning becomes important and large amounts of heat are transferred (Fig. 16) into the upper mixed layer. The oceanic treatment has less effect on the retreat phase, which is somewhat unrealistic, with both models showing an excessive decay in August. There is also a slightly larger-than-observed decay in June, with the somewhat reduced ice thickness in the full model abetting this process. One possibility for this enhanced decay is lack of consideration of snow cover, which field observations have shown to be especially large in this region. Another possibility is an oversimplified treatment of the ther-

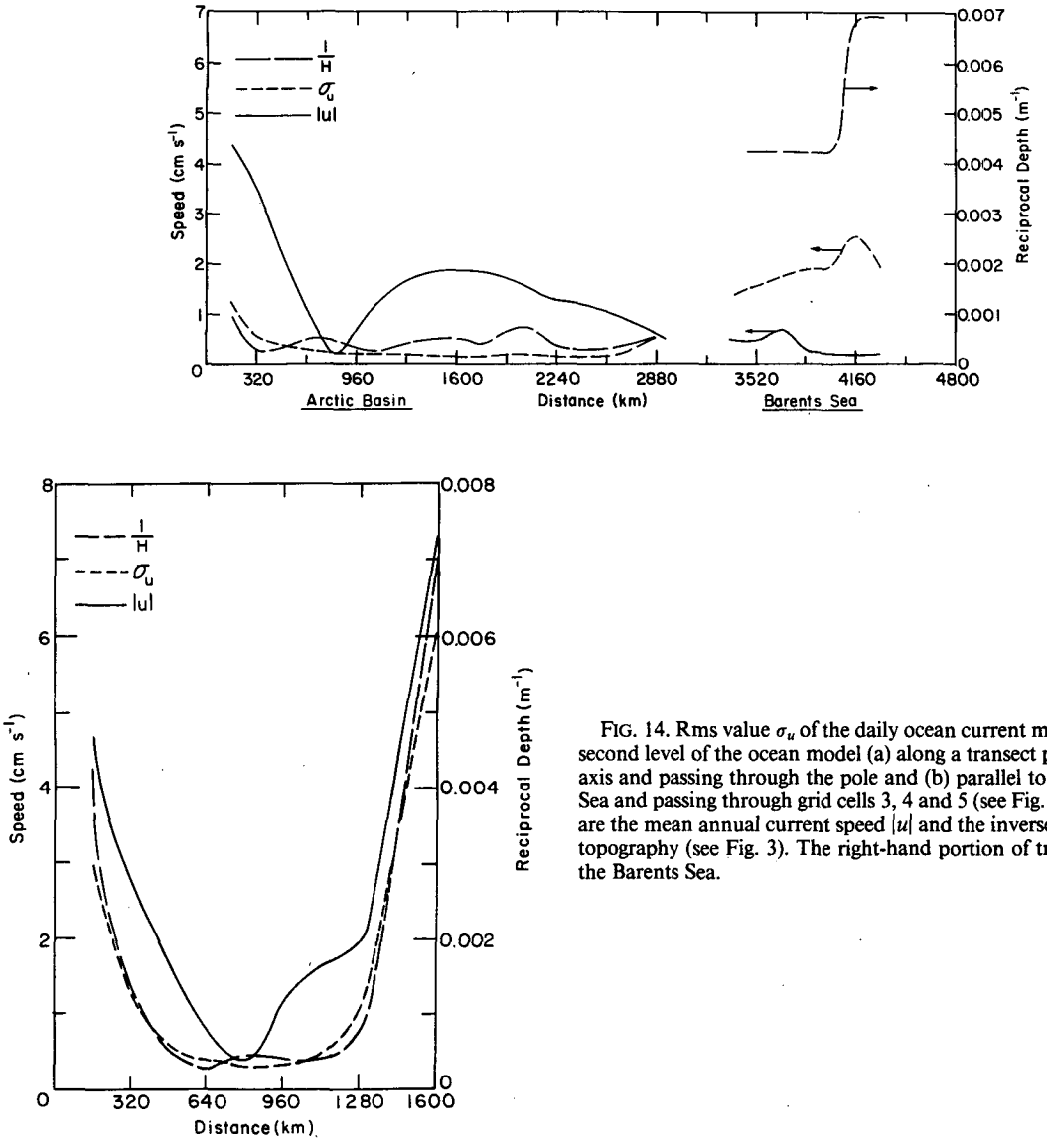

FIG. 14. Rms value σ_u of the daily ocean current magnitude at the second level of the ocean model (a) along a transect parallel to the x axis and passing through the pole and (b) parallel to the Greenland Sea and passing through grid cells 3, 4 and 5 (see Fig. 3). Also shown are the mean annual current speed $|u|$ and the inverse of the bottom topography (see Fig. 3). The right-hand portion of transect (a) is in the Barents Sea.

modynamics of a variable thickness cover. In reality, the distribution of ice thickness is much more complex than the two-level model used here, and the growth of sea ice may be systematically underestimated.

The large amount of heat flux needed to inhibit this growth is illustrated in Fig. 16, which shows the annual average heat flux into the upper mixed layer from other portions of the ocean. This magnitude of heat flux and the spatial variations are in good agreement with estimates by Bunker (1976) for the North Atlantic. There is, of course, some similarity in the methods here, since Bunker's calculations were based on specifying the sea surface temperature. Here the sea surface temperature is predicted subject to the constraints that the deeper ocean is weakly relaxed to observed temperature and salinity. An important feature of this heat flux is the relatively large value in the Barents Sea, which is created by the northward barotropic currents along the Norwegian coast. Analysis of the overall transport there shows a net influx of water northward at the southern boundary of the Barents Sea, while there is an average outflow of ice. These general features are in agreement with Arctic Ocean mass and salt budget analyses by Ostlund and Hut (1984).

That these heat fluxes are dependent on the lateral transport of heat in the upper portion of the ocean and not just the diagnostic terms in the ocean is demonstrated by the comparison to one-year sensitivity simulations in Fig. 17 without lateral transport and without salt fluxes. In the case of no lateral motion in the ocean in December (even with only a one-year simulation) the ice edge in the motionless model has advanced sig-

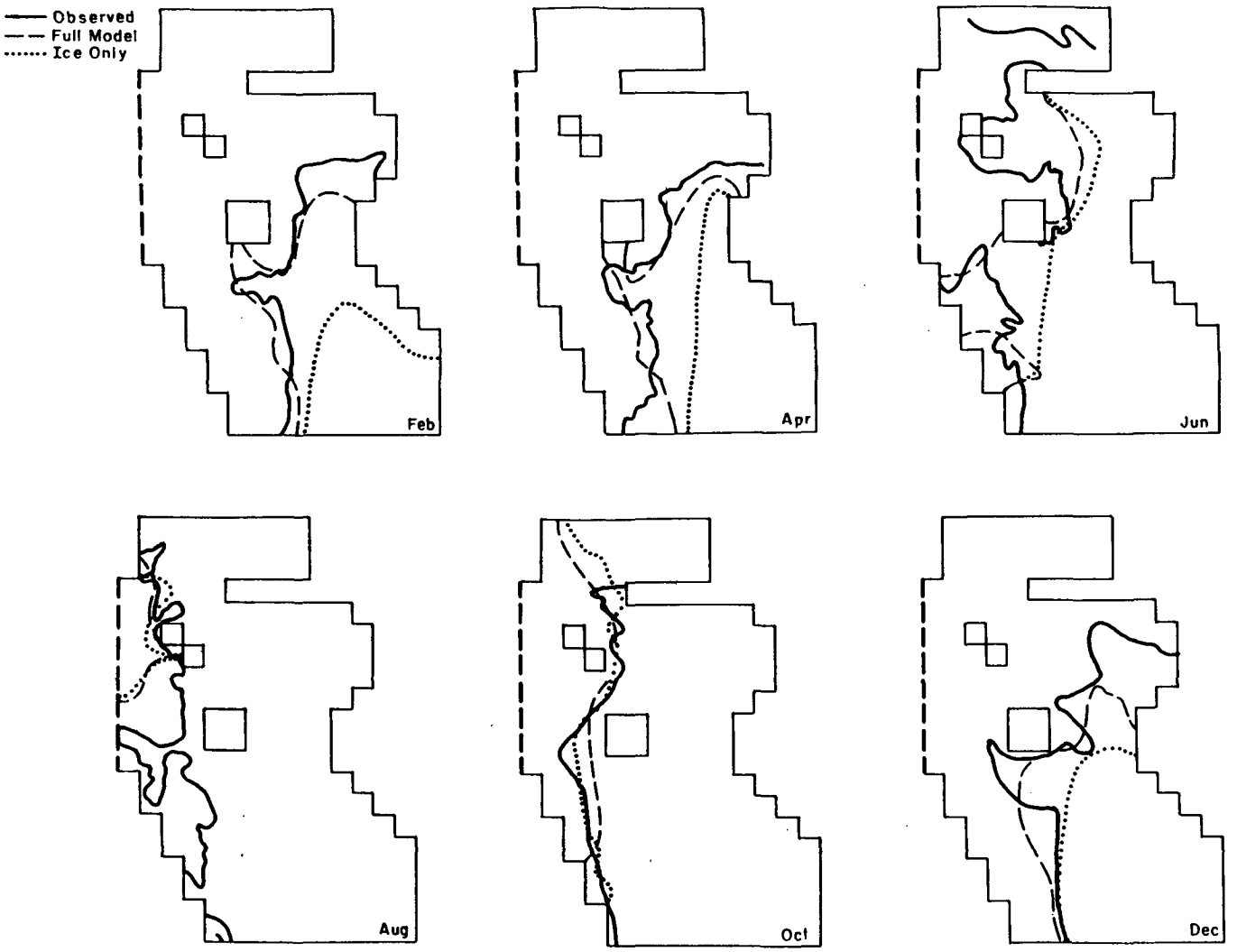

FIG. 15. Simulated and observed 50% concentration limits for both the coupled ice–ocean model and the ice-only model. The observed limits were taken from Fleet Weather (Suitland, Maryland, U.S. Navy) charts for 1979 at the end of the month.

nificantly south and east compared to the full model. Note also that in the half meter contour of thickness, the full model has a thin ice section in the Barents Sea due to the northward heat transport. Basically, the utilization of the weak three-year relaxation time constant gives the model enough freedom for meaningful sensitivity studies of seasonal variations, while still constraining the overall circulation from slowly drifting away from the approximate climatological conditions.

In the case of the no-salt flux sensitivity, there is a reduced advance apparent on day 360. However, the effect here is not as pronounced as the ice advance in the case of no lateral ocean motion, because of the longer time scale needed to establish a freshwater lens. This result does, however, illustrate the importance of the salt flux at the ice edge.

This feature is also demonstrated by a closer examination of the temporal variations of the various fluxes. Such a comparison is shown in Fig. 18, which shows time series of the ice thickness, freshwater flux, ocean–ice heat flux, and atmospheric heat gain at the five numbered grid cells in Fig. 3. The results at grid cell 5 in the Norwegian Sea and grid cell 2 in the central Arctic Basin are the most straightforward, with grid cell 5 having no ice growth or decay, and hence no salt flux; grid cell 2 having very little heat flux.

In the case of grid cell 2 near the pole, this is a location where there is ice all year round and the ocean is very stratified. The behavior here is more in keeping with the classic view of an ice-covered ocean, as, for example, modeled in a one-dimensional mixed layer model by Lemke and Manley (1984). In this instance, due to the strong density stratification, there is very little heat flux, and what there is occurs in the autumn due to the expulsion of salt (a close look at the mixed layer structure shows a deepening of the well mixed

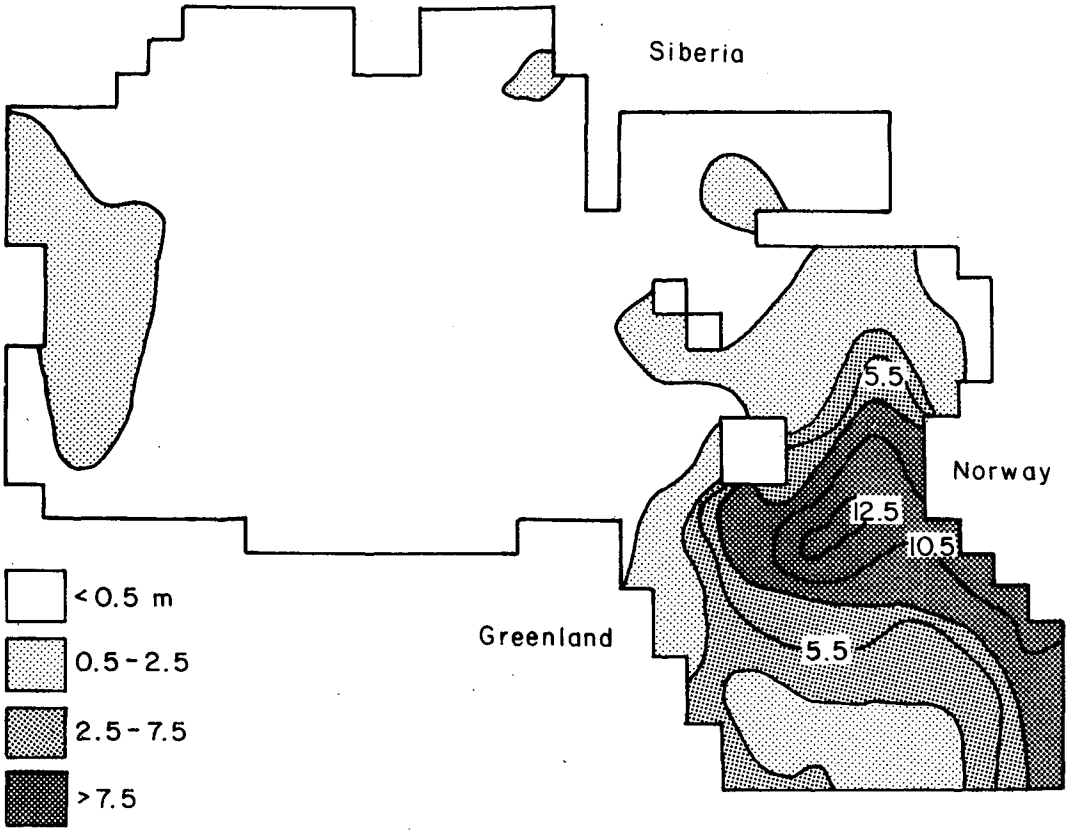

FIG. 16. Average annual heat gained by the upper layer of the ocean from the deeper ocean and by lateral heat transport. The contours are in terms of the melting capacity of the heat in meters of ice per year. For comparison, a melt rate of 1 m of ice per year is equivalent to 9.57 W m^{-2}.

boundary layer into the second level of the ocean model in winter). Because of the small heat flux the atmospheric heat gain is balanced by the ice growth in the fall and the melt in the summer. In this cell the amount of freshwater flux is identical (using appropriate signs) with the ice growth.

The situation for grid cell 1, off the North Slope, is somewhat similar to that at grid cell 2, near the pole. However, due to the disappearance of ice and upwelling there are a number of complicating factors. Although not as large as the fluxes in the Greenland–Norwegian Sea, there is some heat flux here. In the fall this heat flux tends to coincide with the large salt expulsion due to the ice freezing, but continues in the fall due to upwelling of warmer water. Note that the formation of ice and the concomitant insulating effect also tends to cause a very strong decrease in the rate of heat loss in October. The slight rise again in February is likely due to greater wind speed then. This particular grid cell is also affected by the water runoff that is seasonally applied to all perimeter grid cells (to a lesser degree than the main river outflow locations). However, this lasts from mid-June to mid-October and so coincides mainly with the freshwater flux being positive. It does, however, appear to affect the results in September. During this month, comparison of the actual ice melt shows the river runoff to account for about 90% of the freshwater flux. In July, on the other hand, river runoff only accounts for about 10% of the freshwater flux.

Grid cells 3–5 in the Greenland–Norwegian Sea represent a much less stratified ocean (see Fig. 9), and all are more representative of the marginal ice zone region where the dynamic pack ice meets the open ocean. At grid cell 5 there is a simple balance between the atmospheric heat gain and oceanic heat flux. Since there is no ice melt or growth here, differences between these terms are balanced by the warming or cooling of the mixed layer. Note that the oceanic heat flux tends to lag behind the atmospheric heat gain, with the lag being most pronounced in fall as the mixed layer cools off. As this rapid cooling brings the mixed layer close to freezing the rate of cooling slows down (which accounts for the bump in the atmospheric heat gain curve in October). The oceanic heat flux then begins to be very large and only slightly lags behind the atmospheric terms as the mixed layer begins to be warmed in the spring.

Grid cell 4 is mainly a region of large ice melt, with ice thicknesses being very small and alternating day to day with open water. Here there is some density strat-

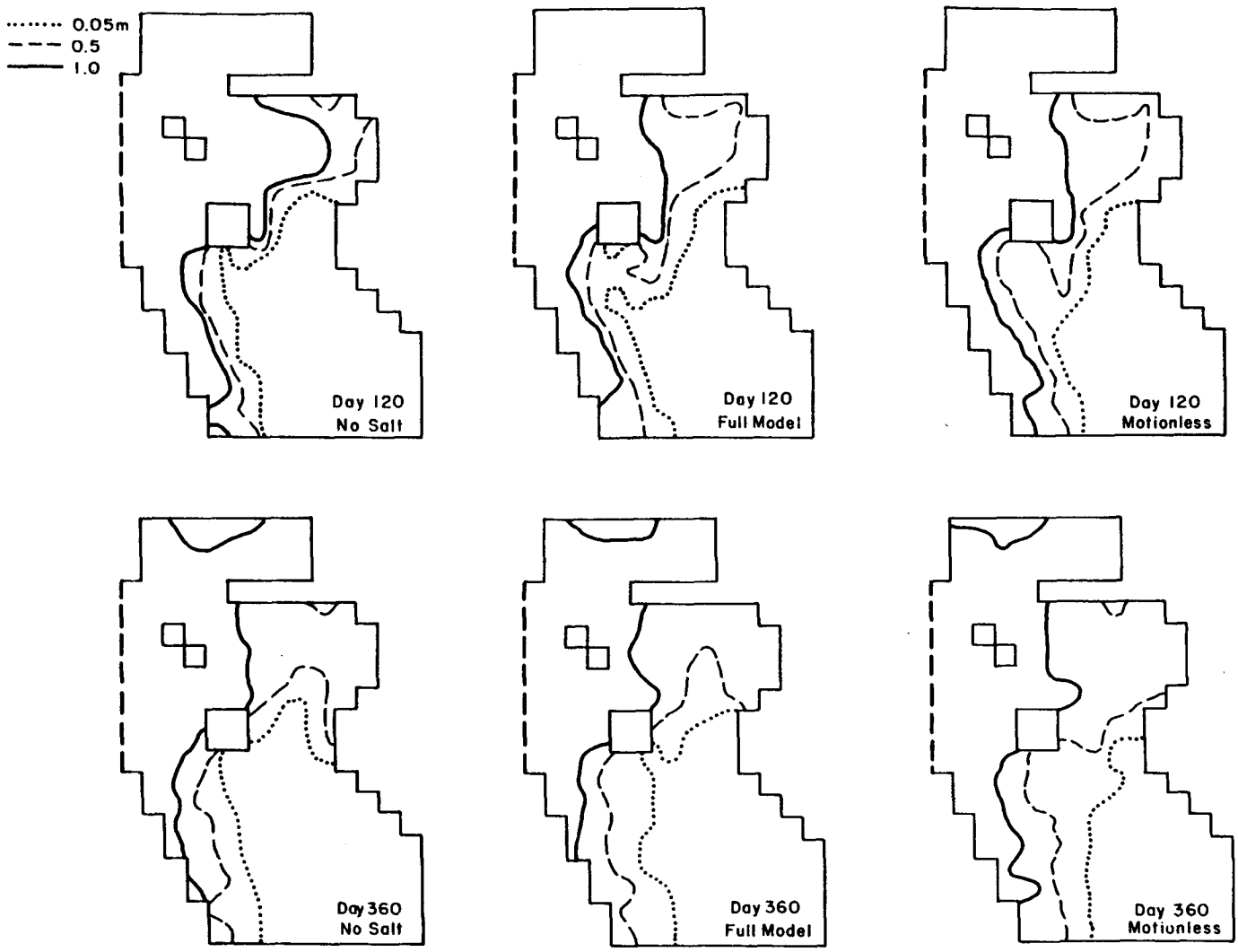

FIG. 17. Ice thickness contours near the ice edge from the full model and the two one-year sensitivity studies on day 120 and day 360.

ification, but not enough to prevent overturning from occurring due to cooling. In particular, although the water above is fresher than the lower water, the lower water is warm enough that a neutral density can be achieved, even though fresher water is being put in at the top. Also, once this overturning occurs the system will become closer to neutral stability and more overturning can proceed. There is in addition very intense atmospheric cooling in this region. As a consequence we see here a much sharper rise in the heat flux, with very high oceanic heat fluxes occurring in February. A closer look at the numbers also shows some boundary layer warming so that there is not always an exact balance between ice melt and the difference between ocean heat and the atmospheric heat gain. This heat flux is initially abetted by a small amount of net ice freezing, but this freezing soon changes to monthly averaged melting as large amounts of ice are advected into the region in the winter as the ice advances. The heat flux decreases as the atmospheric heat gain decreases but maintains a low but positive decreasing value in April, May and June. Since in this analysis heat flux includes any heat advected laterally into the upper layer of a grid cell, this low positive value is likely due to the lateral advection of heat from the warmer surface layers (30 m) to the east.

In many ways this region around grid cell 4 with its deeper convection, large ice melt rates, and almost no ice thickness is similar to the Weddell polynya in the Weddell Sea region of the Antarctic. Analyses of the polynya region (Martinson et al., 1981) have generally made use of a convective adjustment model similar to the one-dimensional portion of this model, but have not explicitly considered advection into the region or lateral oceanic heat as are considered here. In this model the substantial ice advection causes large

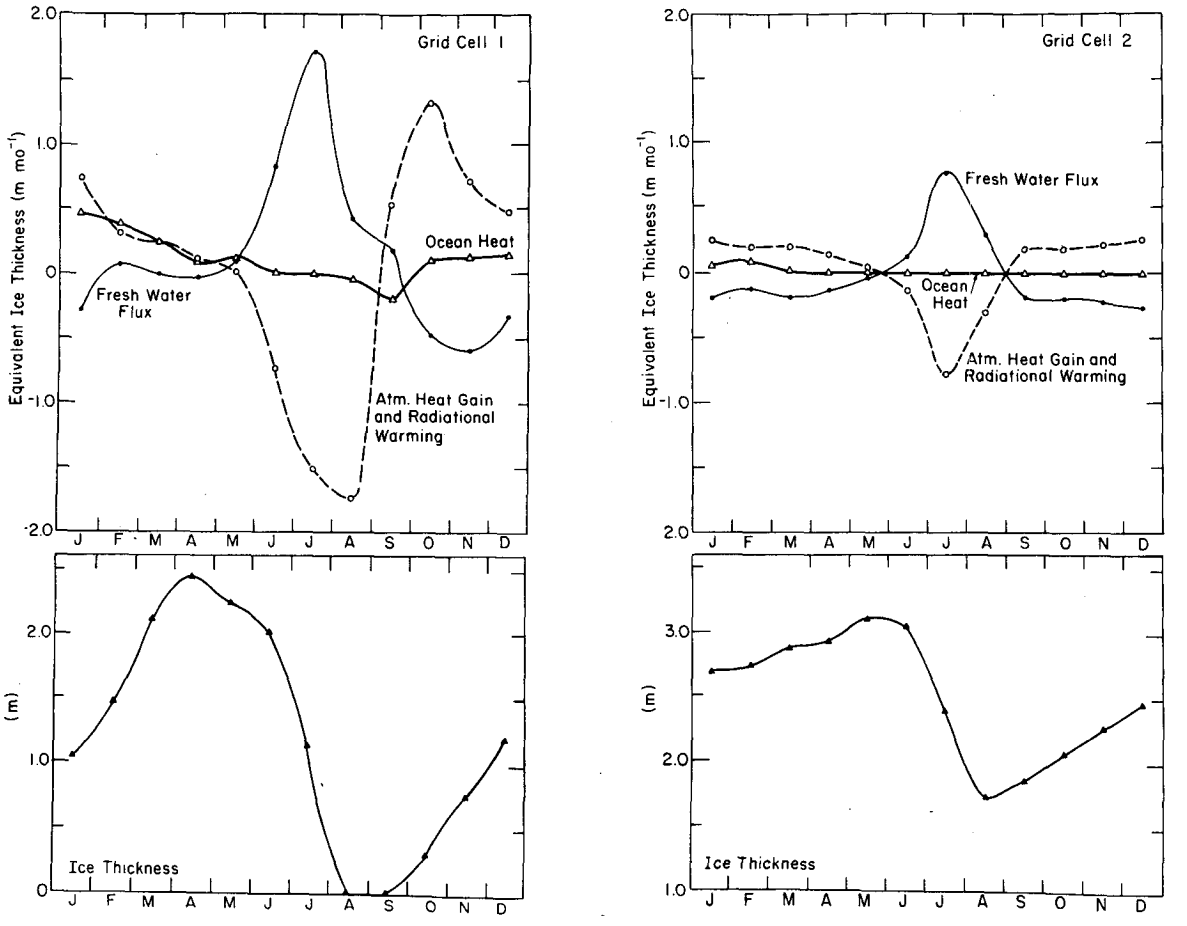

FIG. 18.

amounts of fresh water, which tend to seal off the convection, and allow, on the average, a small ice thickness to exist there. While beyond the scope of this paper, these results demonstrate the utility of this model for investigating the possibly unstable physics of the overturning and highlight the need for a more detailed analysis of a coupled ice–ocean model in the marginal ice zone region.

The final analyzed time series is in grid cell 3, which is inside the East Greenland ice edge with a more stably stratified upper ocean. Here convection is also possible but to a lesser depth. The main feature here is a very close balance between fluctuations of the oceanic heat flux and the freshwater flux. Basically we see a very oscillatory structure, with an increase in heat flux in one month coinciding with an increase in the melting. This oscillatory behavior could be cause and effect, with the increased melting stratifying the system so that the heat flux decreases. This decrease then allows either freezing or lateral advection and diffusion effects to restore the unstable possibilities, and the heat flux goes up again. Lateral advection undoubtedly plays a role here also.

This close balance between ocean heat flux and melting in this region is made possible by the significant ice thicknesses. This can be contrasted to grid cell 4 a bit further east, where thin or often absent ice allows a stronger atmospheric cooling. Note also the very sharp peak in atmospheric cooling in October as the mixed layer goes to freezing and ice forms. However, due to the presence of leads which can fluctuate in time, pulses in atmospheric heat gain can occur. This seems to have occurred in March but was accompanied by larger amounts of oceanic heat flux so that a net melting occurs.

To help clarify these Greenland and Norwegian Sea time series results, Fig. 19 shows the spring and fall vertical temperature profiles. In both grid cells 4 and 5 the heat is essentially taken out of the whole upper column down to at least 600 m. In grid cell 3, however, the stratification is much more pronounced, and there is heat available only down to about 200 meters, which nevertheless is quite a lot more than in the central Arctic Basin, where only heat from the top two layers can normally be obtained. It is also possible for this heat in the upper portion of grid cell 3 to be relatively fre-

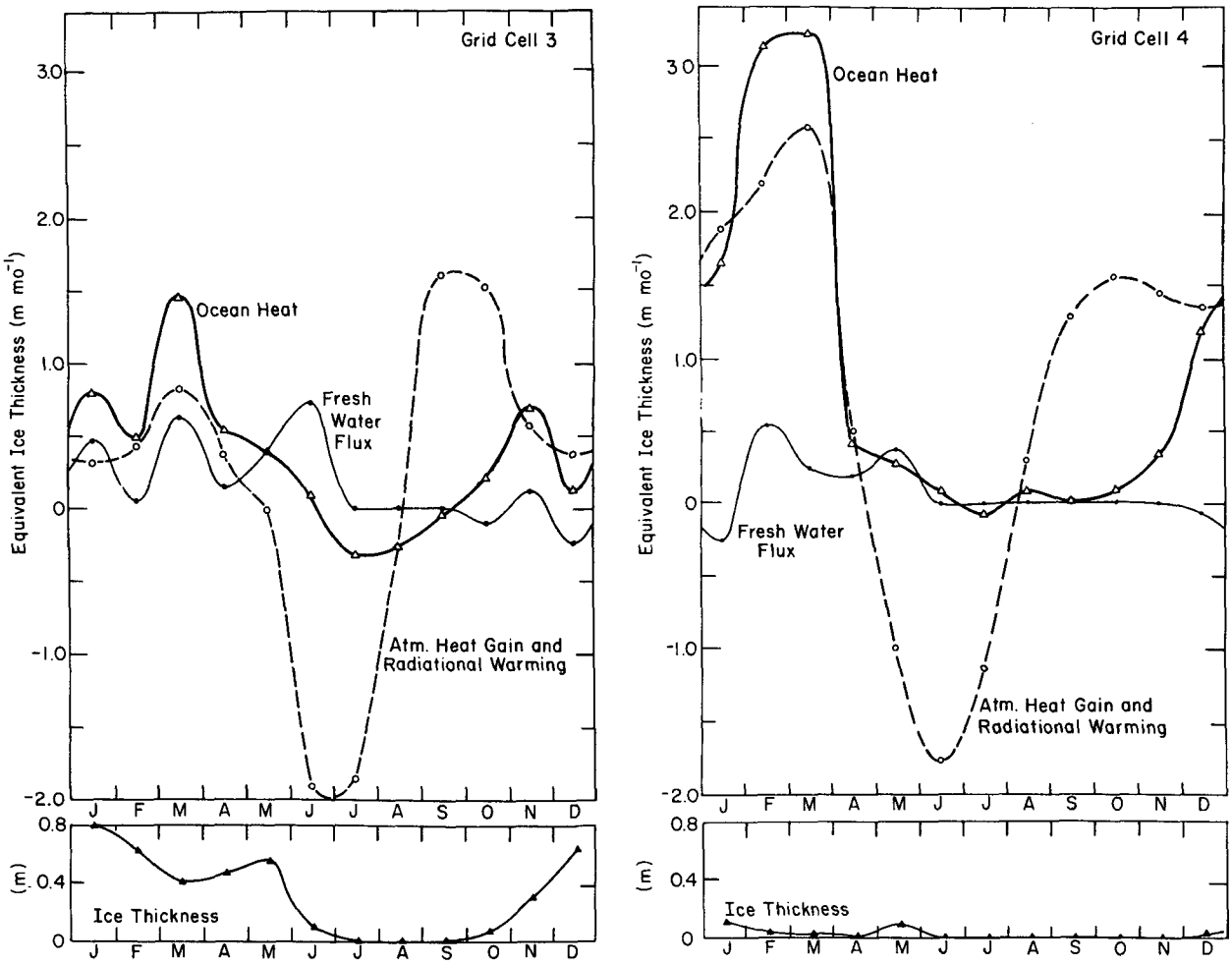

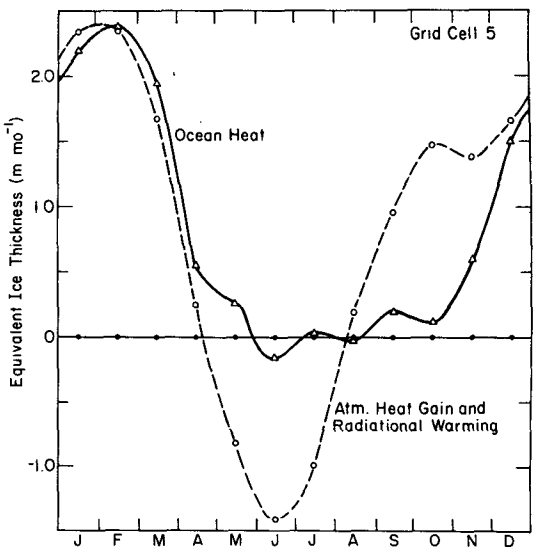

FIG. 18. Time series of the heat budget components for the upper layer of the ocean together with ice thickness and freshwater flux. The dashed line shows the sea-to-air heat exchange, the heavy solid line the oceanic heat flux into the upper level of the ocean, and the light solid line the freshwater flux (negative values represent ice freezing). The fluxes are in units of meters of ice per month. For comparison, 1 meter of ice per month is equivalent to 115 W m^{-2}.

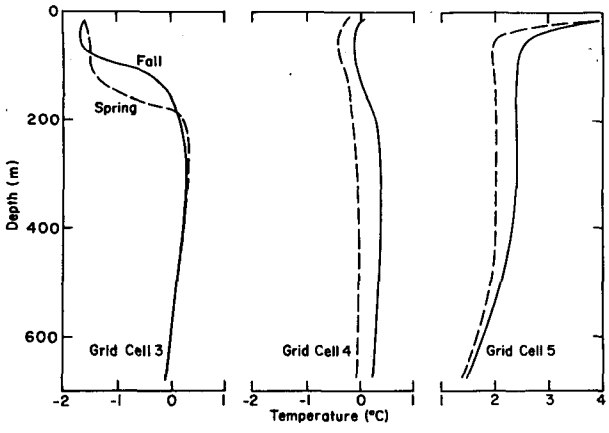

FIG. 19. Seasonally averaged upper ocean temperature profiles for fall and spring in the East Greenland region.

quently replenished by lateral advection from the upper, warmer water to the east, a factor which is undoubtedly important in the maintenance of this warmer upper layer.

Overall, the above analysis helps answer the basic question: What determines the position of the ice edge? In general a coupled atmosphere–ice–ocean model is needed to model the ice edge. In the present case the atmosphere is given, so we can only look at the sensitivity to ice dynamics and ocean circulation. In this context the ice position is largely determined by a competition between ice advection from the north and heat advection from the south, which ultimately reaches the ice mainly through vertical convection. Melting can cause cold fresh water to cap off the warm salty water, but a lot of melting is required to do this. If the ice production increases we expect the front to shift southward.

However, while this overall view is largely correct, as seen above it is substantially complicated by the local ice dynamics and boundary layer processes occurring at the ice margin. It seems plausible that the details of these processes can play a significant role in the advance of the ice margin. For example, the close balance of the heat exchanges at the ice margin (for example, at grid cell 3) indicates that open water may be freezing while thicker ice is melting. Consequently the net salt flux, and hence convection, can hinge on the local ice deformation and advection. Under appropriate conditions the feedback may favor ice melt which could cause a rapidly advancing ice edge. Once formed, the concomitant stratification might be very difficult to remove, and hence the larger scale circulation could be altered.

Clearly, use of detailed satellite imagery in conjunction with modelling experiments and oceanographic measurements from drifting buoys can help clarify the role of these processes in ice edge advance and retreat. However, it also appears necessary to carry out more detailed shipboard investigations of an advancing ice edge. While such studies have been carried out for a decaying ice edge in the MIZEX experiment they have not yet been done on an advancing ice edge.

d. Global balances

From the climatic point of view it is useful to analyze the global surface budgets for the analysis region. This analysis also gives an estimate of the role of the diagnostic terms, since in a purely prognostic simulation the net change of all the surface budgets must be balanced by the inflow terms.

The time series of the vertical exchanges averaged over the analysis region are shown in Fig. 20. In this figure, in addition to the total salt flux time series, we have plotted the ice melt terms. Comparison of these two terms shows how large the river inflow term is.

Overall, these global time series show a form similar to that demonstrated by individual grid cells analyzed above: namely a seasonal variation of both atmospheric heat gain and oceanic heat flux. In the fall the oceanic heat flux lags behind the atmospheric heat flux as the boundary layer must first cool down before any overturning can occur. This rate of atmospheric heat gain then decreases as ice is formed, which provides an insulating effect. The oceanic heat flux begins to grow with the ice formation, making up the difference between the oceanic heat and the atmospheric heat gain. In the summer the heat flux is very small and the melt is essentially due to atmospheric heat losses and radiational warming of the ice and leads.

The rate of melt is much larger than the rate of freezing so that the seasonal cycle of ice mass (not shown) is very asymmetric, with a much sharper decay than growth. It is interesting that, in the decay phase and early freezing period, the salt flux due to river runoff is a very small seasonal term compared to the large

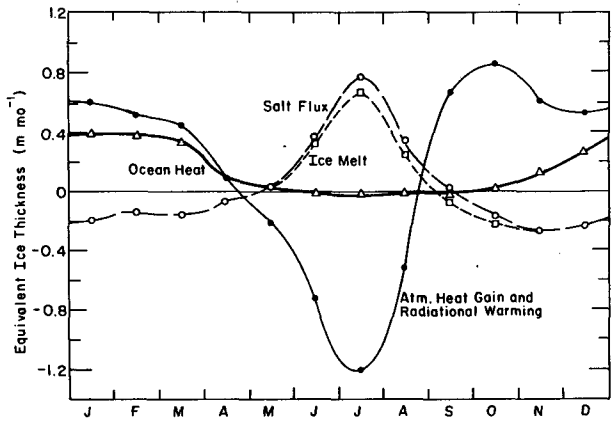

FIG. 20. Globally averaged fluxes into the upper layer of the ocean together with ice melt and total salt flux. The analysis region consists of all grid cells north of the heavy solid line north of Iceland (see Fig. 3) and excludes the hatched grid cells in the Bering Strait region.

TABLE 3. Annual averaged global mass, heat and salt budgets.*

Net freshwater flux	0.30
Net atmospheric heat gain	1.62
Net oceanic heat flux	1.57
Net ice growth	0.06
Northward heat flux through southern boundary	0.54
Northward salt flux	0.14

* Units in equivalent meters of ice per year. For comparison a heat loss of 1.0 m of ice is equivalent to an energy transfer rate of 0.1065×10^{15} watts. Total area of analysis is 0.1113×10^{14} m^2.

seasonal signal due to melting and freezing of ice. However, over a year, the ice melt and freezing terms cancel and one is left with the river runoff. This also means that averaged over the annual cycle, the ocean heat flux essentially balances the atmospheric heat gain. However, it should be cautioned that due to ice advection this is certainly not satisfied locally, since ice can be created at one location and transported to another, an effect which creates very substantial changes in the annual averaged vertical fluxes at a given location (e.g., see Hibler, 1980a).

The degree to which the various temporally averaged global terms cancel is shown in Table 3 where the sums are given. These sums can be compared to the northward transports through the southern boundary north of Iceland, whose spatial and temporal variations are shown in Figs. 21 and 22. The mean annual spatial variations through this boundary (illustrated in Fig. 21) show a qualitative agreement with observed estimates of Dietrich and Worthington reported by Semtner (1976), but with reduced magnitudes. In particular, there is mainly a southward flow through the Denmark Strait of about 1.5 Sv (Sv $\equiv 10^6$ m^3 s^{-1}) and a northward flow of 2 Sv through the Faeroe-Shetland passage. These transports tend to be about a factor of three smaller than Dietrich and Worthington's estimates. This factor of 3 is also about the same discrepancy that occurs within this diagnostic model in terms of the difference between northward heat and salt transports and heat lost to the atmosphere by the ocean or salt lost by the ocean due to river runoff. As a consequence, it seems likely that the northward fluxes simulated in this model are too small by about a factor of three. In particular, Table 3 shows the net heat transport to be about 0.54 m of ice per year, which is about one-third of the 1.569 lost by the ocean. Similarly the northward salt transport of 0.138 is about half of the 0.3 m gained by river runoff. Moreover if we add about 0.2 m of ice equivalent due to snow (not considered here) then this salt transport number would be about one-third of the salt lost by the ocean. (However, these sums do not account for the Bering Sea water.)

The seasonal variations of the salt and heat transports are shown in Fig. 22. These show a seasonal variation of 50% in the northward heat, with somewhat less variation for the salt transport. While much of the salt and heat transport is due to changes of flow transport magnitudes in the Denmark and Faeroe–Shetland passages, a substantial portion of it is also due to changes of some of the intermediate grid cells (sometimes changing signs).

4. Concluding remarks

The basic concept in the diagnostic ice–ocean model described here is to prognostically model phenomena

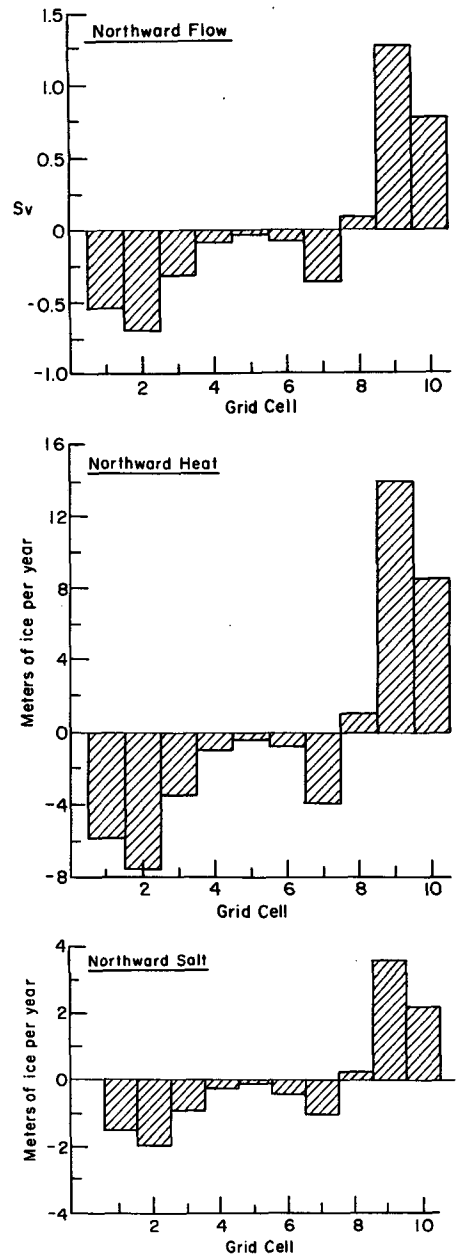

FIG. 21. Spatial variations of an annual averaged northward (a) volume transport, (b) heat transport and (c) salt transport across the southern boundary of the analysis region (denoted by a solid black line north of Iceland in Fig. 3).

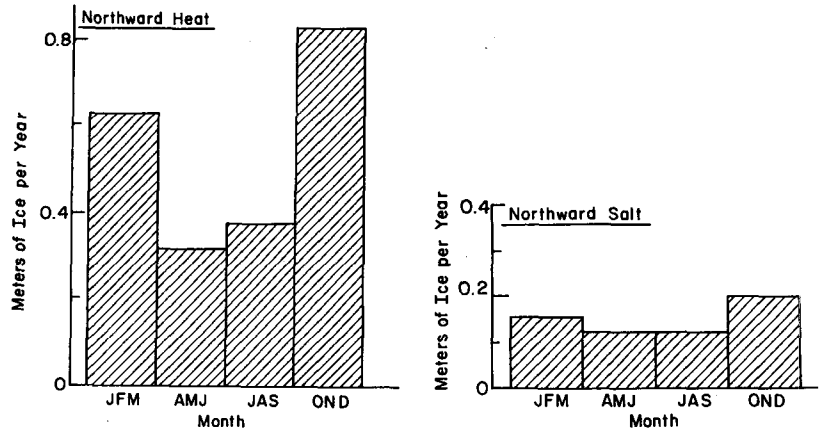

FIG. 22. Seasonally averaged heat transport (a) and salt transport (b) across the southern boundary of the analysis region.

on time scales of days to seasons in a manner consistent with available climatological ocean data. Probably the greatest advantage of this "robust diagnostic" method is its ability to assimilate climatological ocean temperature and salinity data while still simulating seasonal and shorter term variations. This is to a large degree effected by modeling the upper mixed layer and the air–sea heat, salt, and momentum exchanges by a full dynamic thermodynamic sea ice model rather than diagnostically specifying these exchanges. The time constant used here is also important. In particular, while the magnitude of the time constant may not critically affect the magnitude of the correction introduced by the diagnostic terms, how rapidly these correction terms vary does depend on the constant chosen. Because of the three-year equilibrium time scale and ability to assimilate observed data, this model has particular potential for forecast applications, and interannual variability studies where one is interested in phenomena with shorter time scales than climatic, and where one wishes to constrain the climatological state of the system as closely as possible to observed data.

By utilizing this diagnostic ocean forcing in conjunction with daily and seasonally varying atmospheric forcing it has been possible to simulate a more realistic seasonal ice extent cycle than has been previously accomplished with sea ice models. Analysis of the upper ocean results in the East Greenland region shows the deviations from rough climatological estimates of the upper ocean to be significant. The model-produced deviations here are largely responsible for the improved ice edge results. These same remarks also apply to the upper ocean currents. Geostrophic currents in both the basin and off the coast of Greenland calculated directly from density data are not in as good agreement with observations from more detailed studies of the Arctic as are the model results. Analysis of the ice and ocean velocity evolution shows much of the geostrophic adjustment of the ocean velocities to occur early in the simulation and to be due to the inconsistency between the geostrophic currents and the observed density fields. In this context, the diagnostic relaxation creates an "inverse" model.

Although significantly affected by the ocean currents in the long term, the ice motion tends to be much more wind-driven in nature and responds essentially to fluctuations in the wind field. Thus, except in very shallow seas, the ice motion tends to fluctuate much more rapidly than the ocean currents. On the long-term average, however, the ocean currents account for about 40% of the ice drift. Conversely, an analysis of the average stresses into the ice–ocean system shows the ice interaction term to be very significant and on the average to be about 40% in magnitude of the wind stress. As a consequence the wind stress curl ultimately driving the ocean circulation is significantly different (especially in the Arctic Basin region) than the curl of the unmodified wind stress. The full ramifications of this difference can only really be examined via prognostic simulations.

Analysis of the ice edge advance and retreat of this model shows it to be a sensitive balance between convection and a sealing of the upper ocean by large amounts of fresh water. This situation ranges from the extreme Arctic, where the stratification allows very little heat from the deeper ocean to rise to the upper mixed layer, to the ice-free portion of the Norwegian Sea, where no ice forms due to overturning of the upper 600 m, a fact which effectively means that the whole upper ocean must be cooled before ice can form. In the intermediate region of the ice edge, where both significant melting and overturning occur, the interaction is complex. Here it appears that there is a very fine balance, with initial freezing initiating an intense overturning which can withstand considerable amounts of later melting without becoming stratified. Further in from the ice edge, the system is somewhat more stable, and oscillations tend to occur, with large melting

rates followed by less heat flux followed by more heat flux, etc.

On the larger scale the advance and retreat of the ice edge are maintained by the lateral transfer of heat within the ocean replenishing the heat taken out by advection. While this lateral term is significant, significant contributions are also made by the diagnostic terms. Analysis of the global balances shows that a fundamental problem here is that the northward transports of heat and salt in the Denmark Strait/Iceland/Faeroe-Shetland passage are too small. In particular, the northward transport of heat is only about one-third of that lost by the ocean to the atmosphere. The main reason for this appears to be the sluggishness of the currents, which are somewhat overdamped by the large lateral eddy viscosities. This large damping in the central Arctic Basin is largely offset by the specification of the density field.

This ice–ocean model has proven useful in examining the major effects of ocean circulation on seasonal sea ice simulations. However, detailed comparisons to data have been complicated by the use of climatological temperatures and humidities in the atmospheric forcing, together with the repeating of a particular year's atmospheric wind fields. Use of detailed satellite imagery of the ice edge over a period of several years, together with coincident atmospheric forcing, is one possibility for a more complete verification. Also of particular aid would be relatively continuous buoy obtained temperature and salinity measurements in the upper portion of the Greenland Sea.

The model framework constructed here is general in nature. Only the fact that relaxation terms were added to the conservation equation renders the model diagnostic. It is therefore possible, both by analyzing tendencies and various budgets, to see where major difficulties would arise in prognostic simulations. The most major features in this regard that need to be investigated more fully are the large change in the wind to ocean stress in the Arctic Basin region (due to ice interaction), coupled with the overdamped velocities and somewhat sluggish circulation. Problems with a particular year's atmospheric forcing may also pose difficulties. Prognostic simulations are presently underway to examine how the longer-term ocean circulation is affected by the presence of the ice model. The initial results indicate, however, that to do this will require less damping.

Acknowledgments. The simulations described here were made possible by considerable aid and advice from Mr. Mike Cox on the ocean circulation code. Figures and analysis for this paper were prepared from computer printouts by K. Alversen. We also thank S. Bowen for a careful technical editing of the manuscript and D. Harp for typing several revisions of the manuscript. This work was supported by the Office of Naval Research and the National Oceanic and Atmospheric Administration.

APPENDIX A

Estimation of Advection Errors Due to Spherical Geometry

Because the ice model is formulated in rectangular coordinates while the ocean model is in spherical coordinates there will be some error in the ice mass balance and salt fluxes into the ocean. Specifically, since the ice advection is treated in the rectangular grid, the amount of ice transferred into an ocean grid cell will be somewhat in error. The largest error of this kind will occur at the southern end of the grid, far from the pole, where the spherical terms become more pronounced. In particular, in the Greenland Sea, southward-moving ice is considered to be advected between equal area cells, whereas in fact it is moving from a larger area cell to a smaller area cell on the globe. As a consequence, the ice thickness will be slightly underestimated and, if the ice is melting, the amount of freshwater flux into the ocean is underestimated. How-

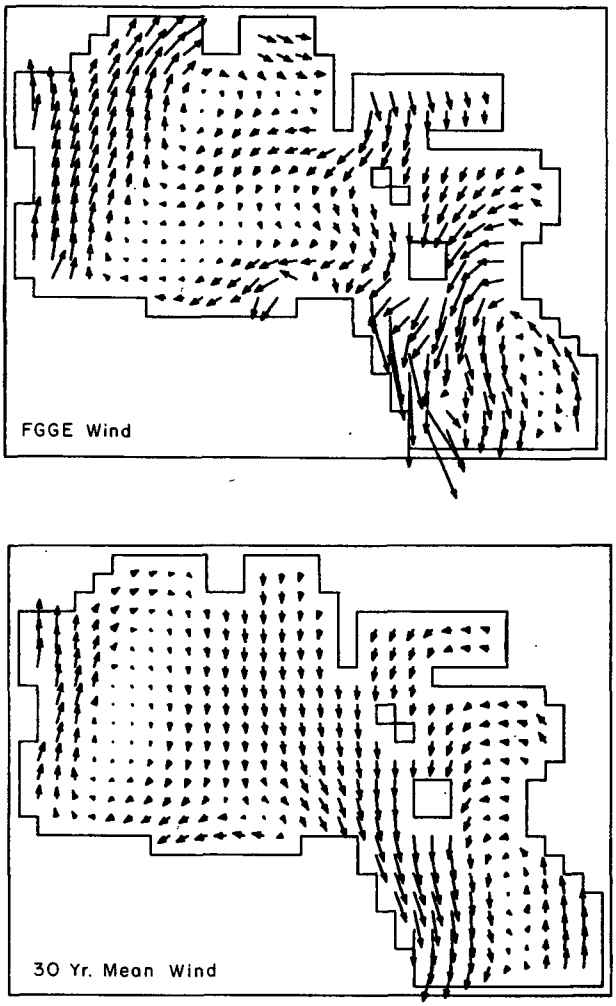

FIG. B1. (a) Mean annual FGGE geostrophic winds, and (b) 30-year mean geostrophic winds over the time period 1951–80. In both plots, a velocity vector one grid space long represents 2.5 m s^{-1}.

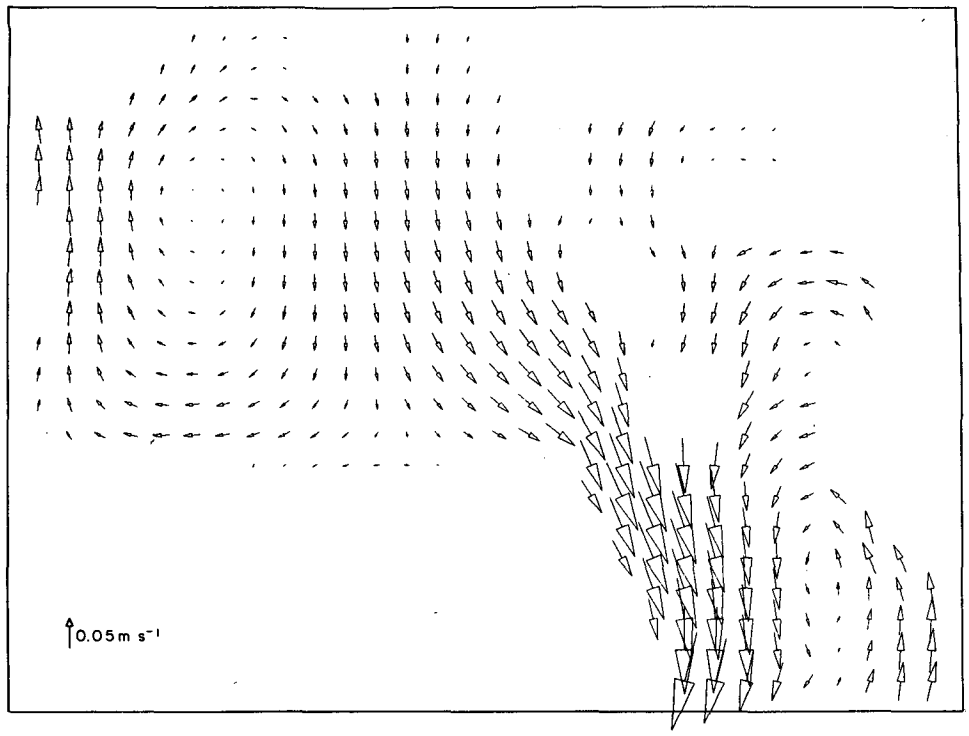

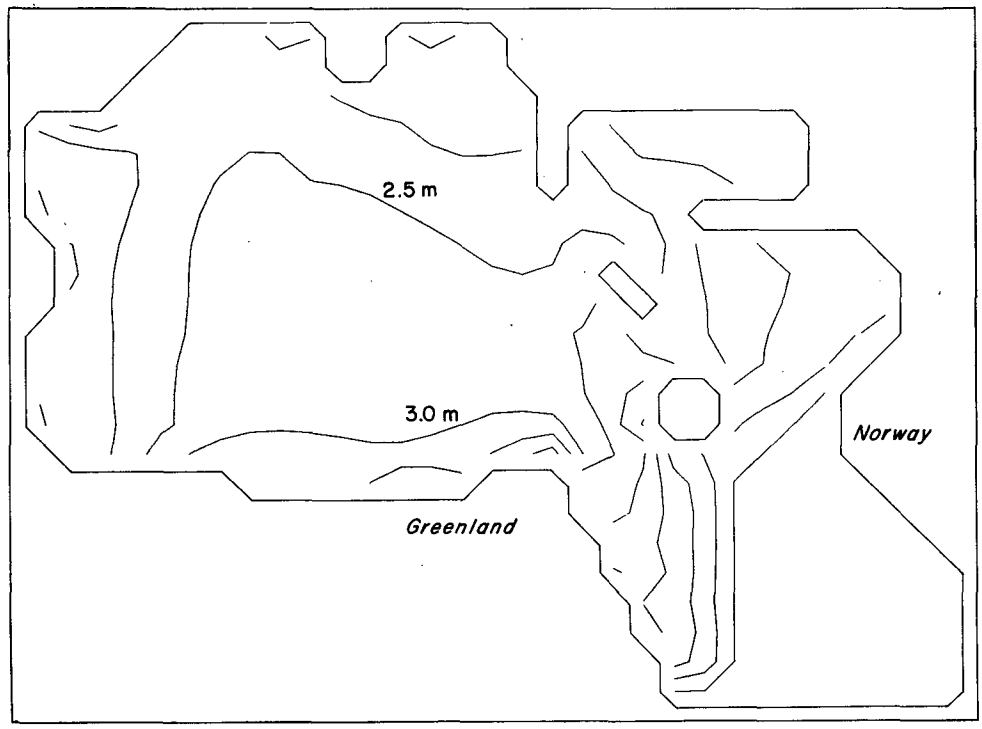

FIG. B2. (a) Mean annual ice drift, and (b) ice thickness contours at the end of December for a one-year ice only simulation using "modified" FGGE winds (monthly means the same as the 30-year averaged wind fields). Part (c) shows the mean annual ice drift using the FGGE winds from the fifth year of the ice only simulation.

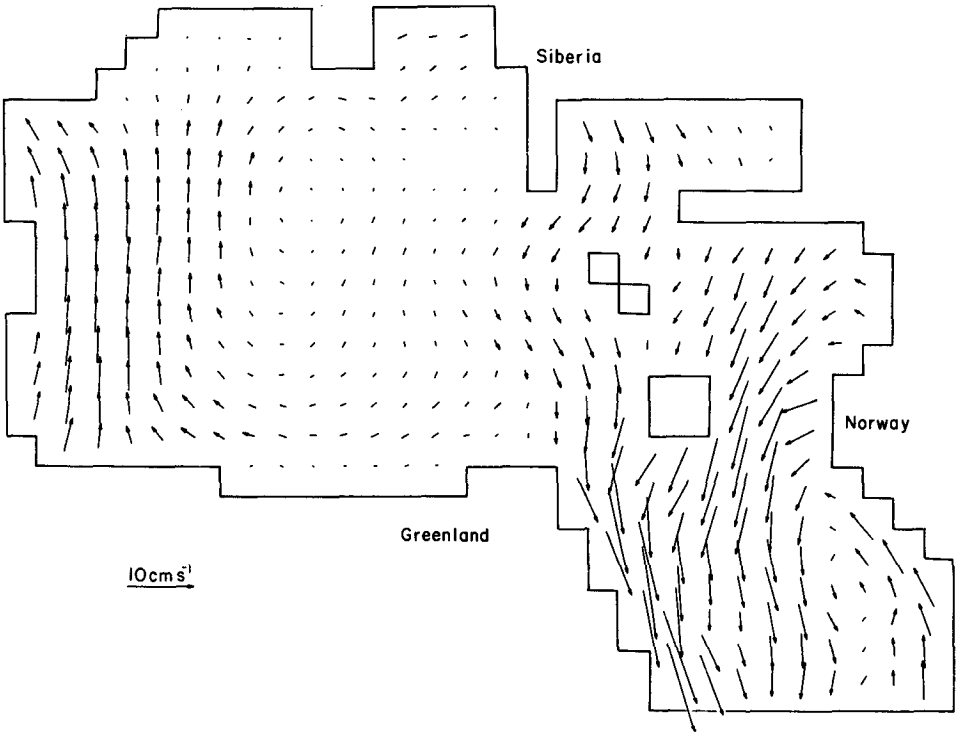

FIG. B2. (*Continued*)

ever, estimation of the upper bound of the magnitude of this error shows it to be at least an order of magnitude smaller than the simulated melt (or ice advection).

Considering the meridional component of advection, the equation in spherical coordinates is given by

$$\frac{\partial h}{\partial t} = -\frac{1}{a\cos\phi}\frac{\partial}{\partial\phi}(\cos\phi vh), \qquad \text{(A-1)}$$

where ϕ is latitude (in our coordinate system with the equator going through the pole), a is the radius of the earth, v the north–south component of ice velocity and h the ice thickness. Carrying out the differentiation this equation becomes

$$\frac{\partial h}{\partial t} = \frac{\tan\phi}{a}vh - \frac{1}{a}\frac{\partial}{\partial\phi}(vh). \qquad \text{(A-2)}$$

Since $a\Delta\phi$ = 160 km the second term is what is calculated in the ice model while the first term is ignored.

To estimate the magnitude of this term we take ϕ = 20°, $a \approx 6 \cdot 10^3$ km, $v = -0.5$ m s^{-1} and $h \approx 3$ m. These constants yield a value of $\Delta h/\Delta t$ of $\approx$0.03 m month^{-1}. Since typical monthly ice advection values (as can be seen by looking at the melting water very near the ice edge in Fig. 18), are of the order of 0.5 m month^{-1}, this error is small.

This factor of 10 also can be estimated by considering the fluxes directly. Basically, the total amount of ice per unit time flowing into the east–west face of a grid cell at latitude ϕ will be proportional to $\cos\phi vh$, whereas the ice model uses vh. The error is then $(1 - \cos\phi)$ ≈ 0.1 for ϕ = 25°, which is about the largest value of ϕ reached over the analysis portion of the grid.

APPENDIX B

Effect of FGGE Winds Versus Climatological Winds on Simulation Results

As discussed in the text, the atypical wind fields occurring during the FGGE year are the main cause of the unrealistic ice buildup occurring in the ice portion of the simulations described here. The essential problem is illustrated in Fig. B1 which compares the mean annual FGGE geostrophic winds to the 30 year mean geostrophic winds taken over the time period 1951–80. The 30 year mean data was compiled (Walsh, private communication; Walsh et al., 1985) from daily NCAR northern hemisphere sea level pressure analyses. As can be seen the mean annual wind displays more of a classic gyre pattern with at least some transpolar characteristics. The FGGE year on the other hand has a much less defined gyre with hardly any transpolar drift. Also in the FGGE year there is a strong component of wind along the Alaska coast toward the Siberian shelf.

To demonstrate that a much more realistic buildup with the 30-year mean winds can be obtained, a one-year ice-only model simulation with "modified" FGGE winds was carried out. The modification consisted of subtracting out the monthly means of the FGGE winds and adding in the 30-year monthly mean wind fields.

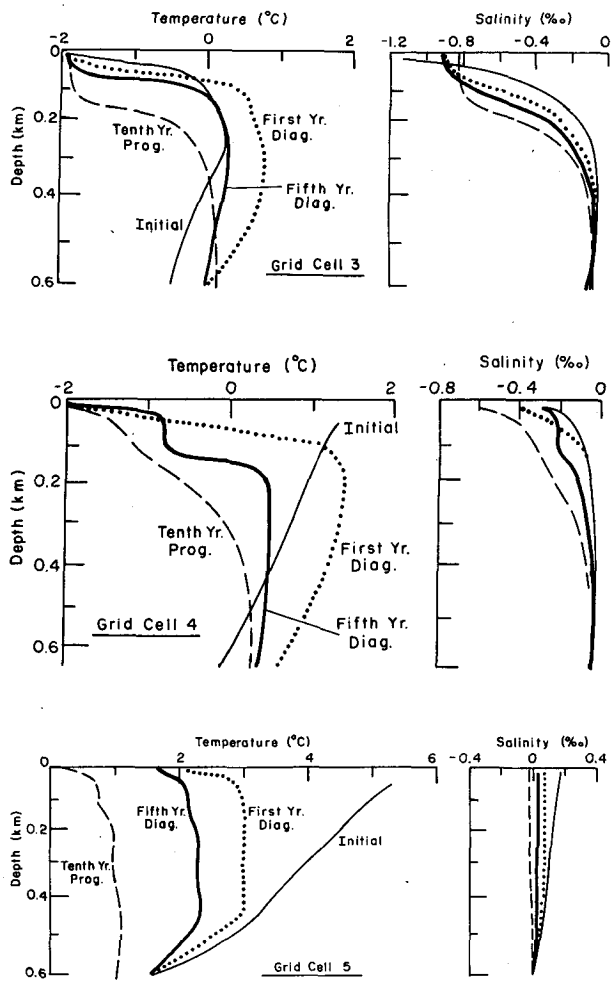

FIG. C1. Salinity and temperature profiles at grid cells 3, 4 and 5 for different simulations. Shown are the initial profile, the profile on day 362, and on day 1 of year five from the diagnostic ice–ocean model. The prognostic profile is on day 1 of year five of a prognostic simulation initialized by the fifth year results of the diagnostic ice–ocean model.

The resulting daily wind fields have realistic daily fluctuations, while still having long-term means closer to climatology. No ocean currents or oceanic heat fluxes were used in the simulation.

Results from this stimulation are illustrated in Fig. B2 which shows the mean annual ice drift and ice thickness contours at the end of December. Also shown in this figure is a vector plot of the ice drift from the fifth year of the ice-only model described in the text. As can be seen the ice buildup using these "climatological" forcing winds is much more realistic than obtained using the FGGE winds, and is more consistent with observed data as reported in Hibler (1980). Also, the ice drift using the "climatological" winds is closer to observed long-term drift patterns than that obtained from the FGGE year, especially as regards the transpolar drift.

APPENDIX C

Effect of Diagnostic Time Constant on Oceanic Adjustment

The main purpose of the diagnostic "damping" term in the ocean model is to constrain the climatological characteristics of the ocean model while still allowing seasonal and shorter term variations to be simulated. Since analysis of the evolution of ocean circulation (section 3a) shows most of the oceanic adjustment to occur in the first two years of the simulation, it does appear that the three year damping constant plays only a minor role in the initial adjustment characteristics of the ocean. However, in the longer term context of full baroclinic adjustment of the ocean model, this damping clearly plays a crucial role by not allowing the temperature and salinity fields to slowly drift away from the diagnostically adjusted fields, which would be expected to take tens of years. In this context, the choice of three years is clearly a compromise: longer than the initial rapid adjustment away from climatology, but shorter than the slower baroclinic drift of the ocean model to its own self determined equilibrium state. This three year time constant also happens to coincide with ice model equilibrium times determined (e.g., see Hibler, 1979) by fitting an exponential to global ice thicknesses versus time.

To help demonstrate these overall assumptions and to lend perspective to the role of the "diagnostic damping," a five year "prognostic" simulation was carried out with the initial conditions taken to be the temperature and salinity values at the end of the fifth year of the diagnostic model. In this prognostic simulation no damping was used in the upper nine levels of the ocean model. (Diagnostic damping was employed in levels ten and below, but since these levels change very slowly, this inclusion has a very minor effect.) Figure C1 shows some of the results from this simulation at grid cells 3, 4 and 5 in the East Greenland region where more of an adjustment was found to occur. For comparison, the fields from the initial conditions and after approximately one year from the diagnostic model are also shown.

Overall the figure shows the prognostic model to drift relatively slowly away from the diagnostic equilibrium fields. Moreover, this drift over five years is generally smaller than the initial adjustment over the first year in the diagnostic model which also leads to qualitative changes in the profiles.

In light of this analysis, it appears that qualitatively similar results to this diagnostic model could have been obtained by integrating a fully prognostic model for only five years from the same initial conditions. Basically the diagnostic terms affect not so much the seasonal character of the model, but rather prevent global imbalances in heat, salt and momentum (as discussed in section 3d) from slowly degrading the modeled baroclinic circulation.

REFERENCES

Bryan, K., 1969: A numerical method for the study of the circulation of the world oceans. *J. Comput. Physics,* **4,** 347–376.

——, 1984: Accelerating the convergence to equilibrium of ocean-climate models. *J. Phys. Oceanogr.,* **14,** 666–673.

——, and M. D. Cox, 1972: An approximate equation of state for numerical models of ocean circulation. *J. Phys. Oceanogr.,* **2,** 510–514.

——, and L. J. Lewis, 1979: A water mass model of the world ocean. *J. Geophys. Res.,* **84,** 2503–2527.

Bunker, A., 1976: Computations of surface energy flux and annual air–sea interaction cycles of the North Atlantic Ocean. *Mon. Wea. Rev.,* **104,** 1122–1140.

Coachman, H. K., and K. Aagaard, 1974: Physical oceanography of Arctic and Subarctic seas. *Marine Geology and Oceanography of the Arctic Seas,* Y. Herman, Ed., Springer-Verlag, 1–72.

Cox, M. D., 1975: A baroclinic model of the world ocean: Preliminary results. *Numerical Models of Ocean Circulation,* Natl. Acad. Sci., USA, 107–120.

——, 1984: A primitive equation, three-dimensional model of the ocean, GFDL Ocean Group Tech. Rep. No. 1, Geophys. Fluid Dynamics Lab./NOAA, Princeton University, Princeton, N.J.

Crutcher, H. L., and J. M. Meserve, 1970: *Selected Level Heights, Temperatures and Dew Points for the Northern Hemisphere.* NAVAIR 50-IC-52, Naval Weather Service Command, Washington, DC.

Hibler III, W. D., 1979: A dynamic thermodynamic sea ice model. *J. Phys. Oceanogr.,* **9,** 815–846.

——, 1980a: Modeling a variable thickness sea ice cover. *Mon. Wea. Rev.,* **108,** 1943–1973.

——, 1980b: Documentation for a two-level dynamic thermodynamic sea ice model. *Spec. Rep. 80-8,* USACRREL, Hanover, NH, 35 pp.

——, 1985: Modeling sea ice dynamics. *Issues in Atmospheric and Oceanic Modeling, Advances in Geophysics,* Vol. 28: *Part A, Climate Dynamics,* S. Manabe, B. Saltzman, Eds., Academic Press, 549–578.

——, and W. B. Tucker, 1979: Some results from a linear-viscous model of the Arctic ice cover. *J. Glaciol.,* **22,** 293–304.

——, and J. E. Walsh, 1982: On modeling seasonal and interannual fluctuations of Arctic sea ice. *J. Phys. Oceanogr.,* **12,** 1514–1523.

——, and K. Bryan, 1984: Ocean circulation: Its effects on seasonal sea-ice simulation. *Science,* **224,** 489–492.

Holland, W. R., and A. D. Hirschman, 1972: A numerical calculation of the circulation of the North Atlantic Ocean. *J. Phys. Oceanogr.,* **2,** 336–354.

Lemke, P., and T. D. Manley, 1984: The seasonal variation of the mixed layer and the pycnocline under polar sea ice. *J. Geophys. Res.,* **89,** 6494–6504.

Levitus, S., 1982: Climatological atlas of the world ocean. *NOAA* **Publ. 13,** U.S. Dept. of Commerce, Washington, DC, 173 pp.

McPhee, M. G., 1978: A simulation of inertial oscillation in drifting pack ice. *Dyn. Atmos. Oceans,* **2,** 107–122.

Manabe, S., and R. J. Stouffer, 1980: Sensitivity of a global climate model to an increase of CO_2 concentration in the atmosphere. *J. Geophys. Res.,* **85,** 5529–5554.

Martinson, D. G., P. D. Killworth and A. L. Gordon, 1981: A convective model for the Weddell polynya. *J. Phys. Oceanogr.,* **11,** 466–488.

Olbers, D. J., M. Wenzel and J. Willibrand, 1986: The inference of North Atlantic circulation patterns from climatological hydrographic data. *Rev. Geophys. and Space Phys.,* submitted for publication.

Ostlund, G. H., and G. Hut, 1984: Arctic Ocean water mass balance from isotope data. *J. Geophys. Res.,* **89,** 6373–6382.

Pollard, D., M. L. Batteen and Y. J. Hass, 1983: Development of a simple upper-ocean and sea-ice model. *J. Phys. Oceanogr.,* **13,** 754–768.

Røed, L. P., and J. J. O'Brien, 1983: A coupled ice–ocean model of upwelling in the marginal ice zone. *J. Geophys. Res.,* **88,** 2863–2872.

Sarmiento, J. L., and K. Bryan, 1982: An ocean transport model for the North Atlantic. *J. Geophys. Res.,* **87,** 395–408.

Semtner, A. J. Jr., 1974: An oceanic general circulation model with bottom topography. *Tech. Rep. No. 9,* Dept. of Meteorology, Univ. of Calif., Los Angeles.

——, 1976: A numerical simulation of the Arctic Ocean circulation. *J. Phys. Oceanogr.,* **6,** 409–425.

——, 1987: A numerical study of sea ice and ocean circulation in the arctic. *J. Phys. Oceanogr.* (in press).

Smith, S. M., H. W. Manard and G. Sharman, 1966: Worldwide ocean depths and continental elevations, SIO Ref. G5-8, Scripps Inst. of Oceanography, University of California, La Jolla, 17 pp.

Thorndike, A. S., and R. Colony, 1982: Sea ice motion in response to geostrophic winds. *J. Geophys. Res.,* **80,** 5401–5413.

Walsh, J. E., W. D. Hibler and B. Ross, 1985: Numerical simulation of Northern Hemisphere sea ice variability, 1951–1980. *J. Geophys. Res.,* **90,** 4847–4865.

Washington, W. M., A. J. Semtner, Jr., G. A. Meehl, D. J. Knight and T. A. Mayer, 1980: General circulation experiment with a coupled atmosphere, ocean and sea ice model. *J. Phys. Oceanogr.,* **10,** 1887–1908.

Willibrand, J., S. G. H. Philander and R. C. Pacanowski, 1980: The oceanic response to large-scale atmospheric disturbances. *J. Phys. Oceanogr.,* **10,** 410–429.

Zubov, N. N., 1943: *Arctic Ice,* 491 pp. [Translation: NTIS AD426972.]